Yttrium aluminum garnet based novel and advanced phosphor synthesized by combustion route activated by Dy, Eu, and Tb rare earth metals

Akshkumar Verma[1,*] (iD), D. P. Bisen[1], Nameeta Brahme[1], Ishwar Prasad Sahu[2], and Arun Kumar Singh[3]

[1] *School of Studies in Physics and Astrophysics, Pt. Ravishankar University, Raipur, Chhattisgarh 492010, India*
[2] *Department of Physics, Indira Gandhi National Tribal University, Amarkantak, Madhya Pradesh 484887, India*
[3] *Department of Physics, Dr. Harisingh. Gour Vishwavidyalaya Sagar, Sagar, Madhya Pradesh 470003, India*

ABSTRACT

In the present studies, rare earth (Dy, Eu, and Tb) activated garnet-based ($Y_3Al_5O_{12}$) phosphors were prepared using the combustion method at 550 °C. The formation of the compounds has been checked by powder X-ray diffraction and structural parameters were calculated. The crystallite/particle size has been measured using Scherrer formula as well as by transmission electron microscopy which show that the size of the particles is in the nanorange. In the photoluminescence emission spectra, YAG:$Dy_{0.05}$ emits two distinctive colors: blue and yellow, YAG:$Eu_{0.05}$ emits red color, whereas YAG:$Tb_{0.02}$ emits green phosphor. Thus, the combination of rare earth ($Dy_{0.05}$, $Eu_{0.05}$, $Tb_{0.02}$) with garnet gives BYRG (blue–yellow–red–green) emissions can produce white light. These discussed phosphors exhibit a strong absorption between 340 and 400 nm. The energy transfer mechanism was also discussed. The higher luminescence color purity (95.68%), Color Rendering Index (95), Correlated Color Temperature (5287 K), and Quantum efficiency (93.7%) are calculated, therefore, synthesized $Y_3Al_5O_{12}Dy_{0.05}Eu_{0.05}Tb_{0.02}$ phosphor material can be used as a WLED phosphor materials in solid-state lighting system.

1 Introduction

There are diverse field of Luminescence, luminescent materials and applications. Modern lighting system totally depends on advanced and novel materials for great efforts for enhancing display quality and visibility [1–3]. In the present scenario, the need and requirement of novel phosphor is one of the most important and urgent challenges to synthesize luminescent material for white light emitting diodes (WLED) for solid lighting devices [4–6]. Other requirement should be fulfillment by modern technology like that maximum quantum efficiency, high

Address correspondence to E-mail: akshverma89@gmail.com

color purity (NTSC), high Color Rendering Index (CRI), cool Correlated Color Temperature (CCT) value, easily availability for WLED application, optimum brightness, Ultra- violet (UV) stability, transparency, and high quenching temperature [7].

A several numbers of Eu^{3+} and Eu^{2+} ion doped phosphors have been synthesized for excellent red and blue luminescence under near-UV excitation respectively, name of few are includes such as $Y_3Al_5O_{12}:Eu^{3+}$ [8], $Y_2O_3:Eu^{3+}$ [9], $YVO_4:Eu^{3+}$ [10], $YPO_4:Eu^{3+}$ [11], $Ca_2ZnWO_6:Eu^{3+}$ [12], $LaPO_4:Eu^{3+}$ [13], $GdAlO_3:Eu^{3+}$ [14], and $Ba_2CaZn_2Si_6O_{17}:Eu_{3+}$ [15] $BaMgAl_{10}O_{17}:Eu$ [16], $ZnS:Ag, Al$ [17], $Y_2SiO_5:Ce$ [18], $KMg_4(PO_4)_3:Eu^{2+}$ [19], $RbBaPO_4:Eu^{2+}$ [20], $Ca_3Mg_3(PO_4)_4:Eu^{2+}$ [21], $LiCaPO_4:Eu^{2+}$ [22], $SrZnP_2O_7:Eu^{2+}$ [23], $SrCaP_2O_7:Eu^{2+}$ [24], $NaMgPO_4:Eu^{2+}$ [25]. Tb^{3+} and Mn^{2+} ions are have found to produce green emission in numerous host compounds [26–30]. Some standard green phosphors have been reported such as $Mg_2SiO_4:Tb^{3+}$ [29], $SrAlSi4N7: Pr^{3+} Sm^{3+} Tb^{3+}$ [27], $MgSrAl_{10}O_{17}: Mn^{2+}$ [28], $ZnGa_2O_4:Mn^{2+}, Cr^{3+}$ [29], $Li_2Mg_{1-x}ZrO_4:xTb^{3+}$ [30], $Zn_2SiO_4:Mn$ [31], $Y_2SiO_5:Tb$ [32], $Y_3Al_5O_{12}:Tb$ [33].

For the developing of best WLED phosphor materials to the single-phase host doped with co-doped rare earth ions and transition metals that operate under ultraviolet or near-ultraviolet excitations numerous efforts have been taken to develop the single-phase host-based phosphor materials for the WELDs [1, 2, 4, 34–36]. Without compromising in the stability and color reproducibility, the use of single-phase phosphor compound for fabricating of WELDs and it will be potentially easy for NUV convertible WLEDs [1]. There are several white color emitting phosphors have been reported such as $BaZn_2(PO_4):Ce^{3+}, Dy^{3+}/Tb^{3+}$ [4], $K_2SrP_2O_7:RE^{3+}(RE = Sm, Tb, Eu, Dy)$ [37], $Ca_8Gd_2(PO_4)_6O_2:(Ce^{3+}/Eu^{2+}/Tb^{3+}/Dy^{3+}/Mn^{2+})$ [38], $LaPO_4:RE^{3+}$ (RE = Eu, Tb, Dy, Ce) [39], $Mg_{21}Ca_4Na_4(PO_4)_{18}:Dy^{3+}Tb^{3+}Eu^{3+}$ [40], $Zn_2SiO_4:Mn^{2+}-Eu^{3+}-Dy^{3+}$ [41], $Sr_3Gd(PO_4)_3:Dy^{3+} Eu^{3+}$ [42], and $Sr_2SiO_4 : Dy^{3+} Mn^{2+}$ [43].

Garnets (YAG) based phosphor materials have some outstanding properties such as good stability, Optimum brightness, high chemical stability, Low energy consumption, long life span, High thermal stability, and Friendly environments [8, 33, 44–50]. The garnets (YAG) based phosphor are used as hosts

with doping rare earth ions for luminescent application [1, 47]. The White-LEDs (W-LEDs) already have been produced by the combination of garnet $Y_3Al_5O_{12}:Ce^{3+}$ phosphor and chips of InGaN [51]. The $Y_3Al_5O_{12}$ based phosphor materials can behave as photo-luminescence, thermo-luminescence material, electroluminescence, and cathodo-luminescence [44, 52–56]. On the basis of the emission spectra of the rare earth ions, the combination of Dy^{3+}, Tb^{3+}, and Eu^{3+} in YAG is expected to produce a white light spectrum [50, 53, 57–61]. Therefore, in the present studies, we synthesized $Y_3Al_5O_{12}$-based phosphors doped with Dy, Eu, and Tb rare earth activators by the combustion method using urea as fuel.

2 Preparation techniques

In the present work, we synthesized YAG:Dy, YAG:Eu, YAG:Tb, YAG:Eu, Dy, and YAG:Eu, Dy, Tb phosphors compounds for WLED applications. The combustion synthesis process is similar as explained in Refs. [59, 60]. Aksh et al. were already used combustion synthesis for synthesizing various aluminates [57–61]. The nitrates (oxidizer) and urea (fuel) ratio were calculated by the techniques designated as previous. In this work, stoichiometric amounts of $Y(NO_3)_3 \cdot 6H_2O$, $Al(NO_3)_3 \cdot 9H_2O$, $Dy(NO_3)_2 \cdot 6H_2O$, $Eu(NO_3)_2 \cdot 6H_2O$, $Tb(NO_3)_2 \cdot 6H_2O$, and NH_2CONH_2 were taken and carefully mixed. In this present work, we were used 1 h mixing time of the raw material before heating. After regular mixing of raw materials A thick paste is formed. The alumina crucible with thick paste was introduced in a preheated furnace maintained at 550 °C. after 1–2-min exothermic combustion reaction (Eq. 1) crucible was removed outside the furnaces and grind 1 h, the foamy product. Similarly, all other materials were synthesized by combustion route Fig. 1S, synthesized material is listed in Tables 1 and 1S.

$$3Y(NO_3)_3 \cdot 6(H_2O) + 5Al(NO_3)_3.9(H_2O)$$
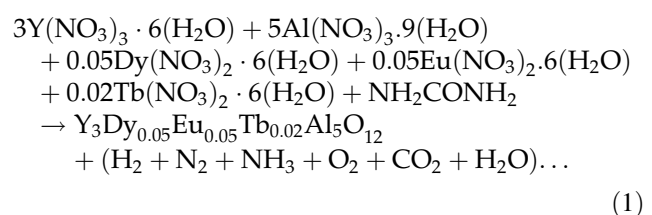$$+ 0.05Dy(NO_3)_2 \cdot 6(H_2O) + 0.05Eu(NO_3)_2.6(H_2O)$$
$$+ 0.02Tb(NO_3)_2 \cdot 6(H_2O) + NH_2CONH_2$$
$$\rightarrow Y_3Dy_{0.05}Eu_{0.05}Tb_{0.02}Al_5O_{12}$$
$$+ (H_2 + N_2 + NH_3 + O_2 + CO_2 + H_2O)\ldots$$

$$(1)$$

Table 1 The various samples synthesized by the urea fuel combustion (UFC) process

Sample code	Synthesized sample
YAG-Host	$Y_3Al_5O_{12}$
YAG:Dy	$Y_3Al_5O_{12}:Dy_{0.05}$
YAG:Eu	$Y_3Al_5O_{12}:Eu_{0.05}$
YAG:Tb	$Y_3Al_5O_{12}:Tb_{0.02}$
YAG:DyEu	$Y_3Al_5O_{12}:Dy_{0.05}Eu_{0.05}$
YAG:DyEuTb$_{0.01}$	$Y_3Al_5O_{12}:Dy_{0.05}Eu_{0.05}Tb_{0.01}$
YAG:DyEuTb$_{0.02}$	$Y_3Al_5O_{12}:Dy_{0.05}Eu_{0.05}Tb_{0.02}$
YAG:DyEuTb$_{0.03}$	$Y_3Al_5O_{12}:Dy_{0.05}Eu_{0.05}Tb_{0.03}$
YAG:DyEuTb$_{0.04}$	$Y_3Al_5O_{12}:Dy_{0.05}Eu_{0.05}Tb_{0.04}$

## 3 Characterization instruments details

Structural and crystallinity analysis were investigated by as Powder X-ray Diffractometer (PXRD), result of (D8 ADVANCED BRUKER). The surface morphology, EDX (Energy Dispersive X-ray Spectroscopy) mapping, crystallite size, and SAED pattern were observed using field emission scanning electron microscopy (SEM, FEI NOVA NANO SEM^{TM} 450) and transmission electron microscope (TEM, TEC-NAI G^2 T30, S-TWIN). Fourier transform infrared spectroscopic (FTIR) studies were recorded by 84,005 (SHIMADZU), with a resolution of 2 cm^{-1}. The range of 500–3800 cm^{-1}. (Sample mixed with KBr in 1:5 ratio) used for identification of homogeneity, purity and for structural properties analysis. Raman Spectra recorded by Raman micro spectrometer RENISHAW in via Raman microscope (He–Ne Laser 633 nm, Ar laser 514 nm). Photo-Luminescence (excitation & emission) spectra were recorded by RF- 5301 PC Shimadzu Spectro-fluorophotometer, hitachi F-4500 florescence spectrometer. De-cay curve recorded by RF-5301 PC Shimadzu Spectro-fluorophotometer. The PL quantum yield (efficiency) of synthesized sample were measured under UV-violet excitation (500 W Xe lamp) using an integrating sphere.

4 Result and discussion

4.1 Structural and crystallinity analysis

All YAG, YAG:Dy, YAG:Eu, YAG:Tb, YAG:Dy Eu, and YAG:Dy, Eu, Tb synthesized samples were measured and analyzed by PXRD. The PXRD pattern

of all selected synthesized compounds are revealed in Fig. 1 with comparing the PXRD patterns with standard JCPDS card no. 33-0040 [7, 33, 50, 53]. However, there are some weak diffraction peaks from the impurity phase and effect of doping of Dy, Eu, and Tb. This small amount of Dy, Eu, and Tb does not change the structure of host material (YAG). However, the shift of diffraction angle is detected with addition of Eu^{3+}, Dy^{3+}, and Tb^{3+} which revealed Fig. 2(a–c). The crystalline size and crystallinity are played important role in the maximum luminescence efficiency and other luminescence properties of synthesized materials [53]. In this case all synthesized phosphors exhibited the formation of sharp diffraction pattern is the consequence of the generation of high improved crystallinity. The structural parameters such as lattice constant (a), inter-planner spacing(d) is calculated by Bragg equation, average crystallite size (D_s) and (D_{W-H}) is calculated by Debye Sherrer (Eq. 2) and Hall–Williamson method (Eq. 3) respectively. The micro-strain (ε) and dislocation density (δ) is calculated (Eqs. 4 & 5) from the XRD data for the main peak of at [420] (Fig. 2S) [62, 63], all the calculated values are listed in Table 2. Figure 3 shows the typical micro-strain plot of discussed materials. The minimum value of dislocation density (δ), and micro-strain (ε) indicates that observed crystallinity of materials is suitable for luminescence application. The estimated crystallite size of YAG based phosphor is found to increase with Eu, Dy, and Tb doping, larger crystallite size decreases the density of the grain boundaries, which
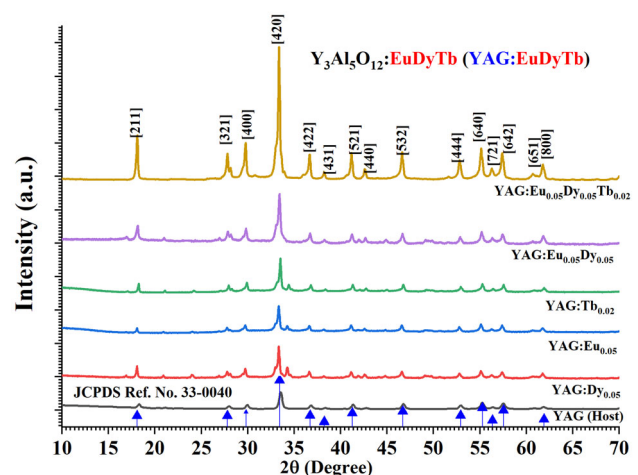
Fig. 1 Typical PXRD graph of synthesized garnet samples doped with rare earth metals
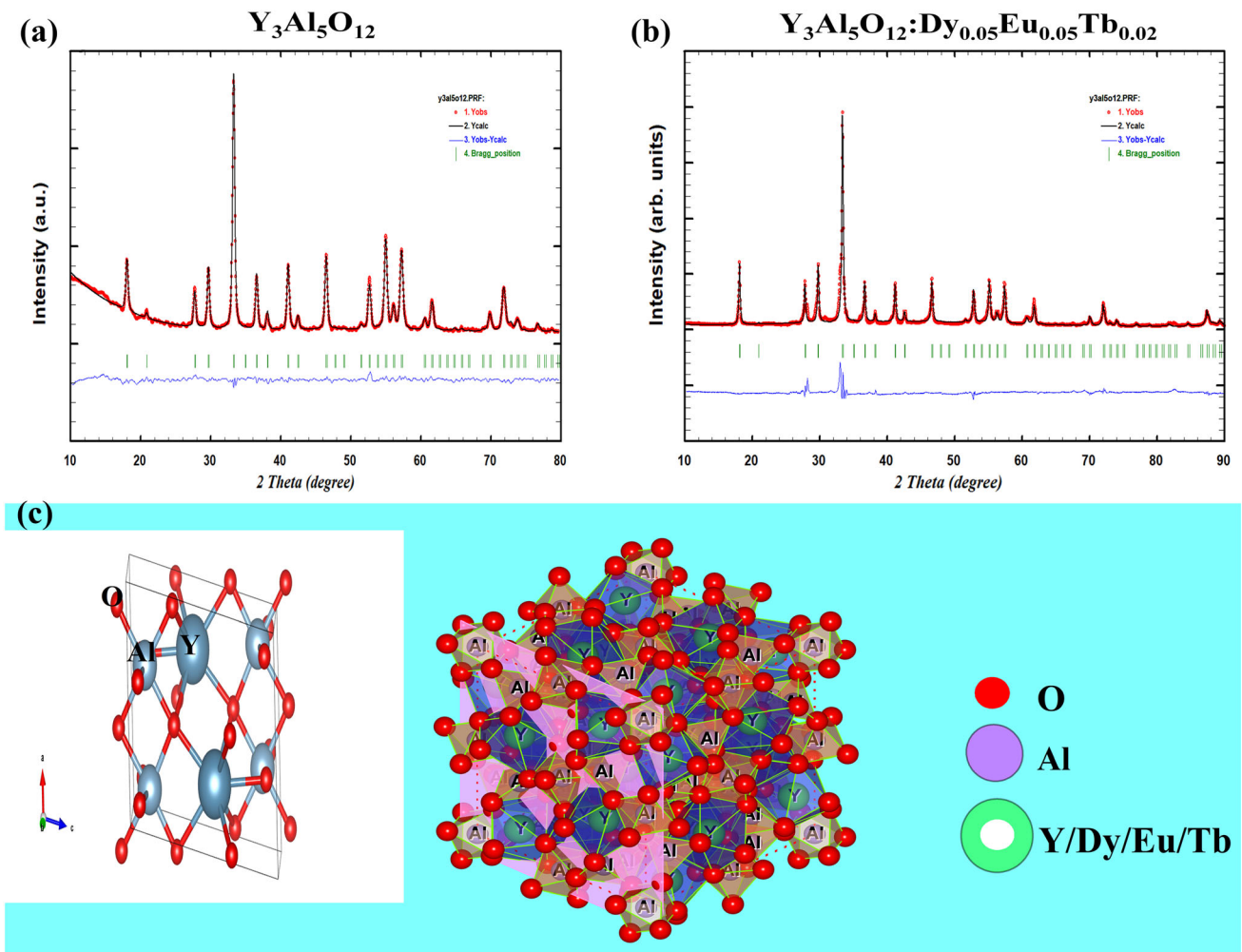
Fig. 2 **a–c** Typical Rietveld refinement curve of YAG & YAG: DyEuTb$_{0.02}$, and **c** cubic crystal structure for YAG:DyEuTb$_{0.02}$ sample

Table 2 Typical values of peak angles, FWHM, d-spacing, crystallite size, dislocation density, and macrostrain of YAG:Dy$_{0.05}$Eu$_{0.05}$Tb$_{0.02}$ phosphor

Sample	2θ (Degree)	β	d	D_s	δ	D_{W-H}	Micro strain (ε)
YAG	33.55900	0.006970	0.266820	20.77458	0.00231	22.3905	0.001660
YAG:Tb	33.33850	0.004700	0.268540	30.78926	0.00070	38.8081	0.000900
YAG:Eu	33.52210	0.004020	0.267110	36.01029	0.00124	30.5890	0.001220
YAG:Dy	33.43299	0.005099	0.267803	28.38900	0.000856	36.8101	0.001014
YAG:DyEu	33.33950	0.004230	0.268533	34.17030	0.001050	33.1677	0.001125
YAG:DyEuTb$_{0.02}$	33.36907	0.004030	0.268301	35.83870	0.000778	61.9519	0.000967

might scatter light generated inside due to enhancement the photo-luminescence properties.

$$D_S = \frac{0.9\lambda}{\beta\cos\theta} \tag{2}$$

The peak broadening in of synthesized samples originates not only due to crystallite size but also due to existing strain. Dislocation density (δ) is calculated by Eq. (5).
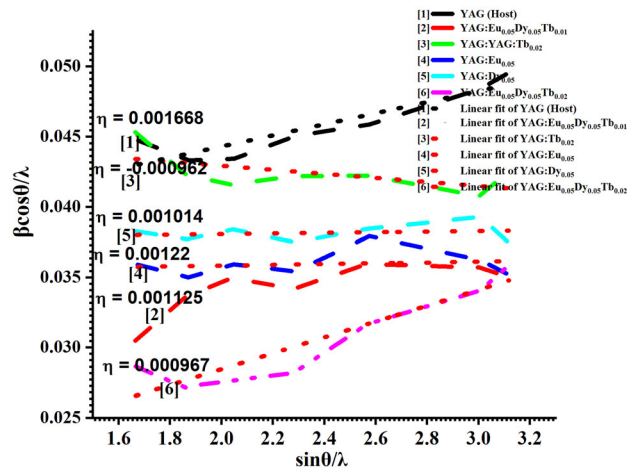
Fig. 3 Typical micro-strain plot of $Y_3Al_5O_{12}$:Dy, Eu, Tb samples

$$\beta cos\theta = \frac{k\lambda}{D_{W-H}} + \epsilon sin\theta \tag{3}$$

Where, D_{W-H} = average crystallite size, B = is the FWHM, ϵ = micro-strain, θ = angle of diffraction, and λ = wavelength of the X-ray radiation.

$$\epsilon = \frac{\beta cos\theta}{4} \tag{4}$$

$$\delta = \frac{1}{D_S^2} \tag{5}$$

A structural refinement using PXRD data of the synthesized YAG:DyEuTb$_{0.02}$ compound by Rietveld method using full prof software was performed to analyze the structural and unit cell parameters of the discussed materials were shown in the Fig. 2(a, b) and refinement parameters were tabulated in Tables 3 and 4. By using the pseudo-voigt function we have refined PXRD data of the YAG and YAG:DyEuTb$_{0.02}$ sample by computing the Bragg contribution (χ^2) and goodness of fit (GOF) parameters [7, 57]. This GOF is subjected to some radiality factor of R_{wp} and R_{exp}, GoF = R_{wp}/ R_{exp}. The χ^2 must be < 5 and GoF must be approach to unity for perfect refinement of PXRD data of samples. In this work, GOF and χ^2 were calculated and found 1.1860 and 3.7, respectively, for YAG:DyEuTb$_{0.02}$ phosphors. The result designates good agreement among the observed and calculated by XRD pattern. Figure 2c shows the crystallographic structure of garnet was described as a 3D structure of polyhedrons, in which tetrahedron (AlO$_4$) and octahedron (AlO$_6$) are linked by shard oxygen ions. The Y^{3+} ions are an eight co-ordinated dodecahedral (YO$_8$) arrangement in the three crystallographic directions. The Dy^{3+}, Eu^{3+}, and Tb^{3+} ions when incorporated in the lattice goes and occupy the Y^{3+} site. The lattice parameter is calculated from the least square fitting of the XRD peaks, and are found 12.0393Å for doped YAG:DyEuTb$_{0.02}$ material and 12.0069Å for undoped YAG materials. The lattice parameters for the doped samples compared to the undoped samples are increased due to different and more ionic radii of rare earth (Dy^{3+} = 0.091 nm, Eu^{3+} = 0.106 nm, and Tb^{3+}= 1.18 nm) ions as compared to Y^{3+} (0.1011 nm) ions. Therefore, the Dy^{3+}, Eu^{3+}, and Tb^{3+} ions are expected to mostly enter into the distorted dodecahedral by exchanging the Y^{3+} (24c) ions [7, 33, 50]. In the garnet structure (complex structure) activators and co-activators are accommodated at different location or position of dodecahedral site, In a local view each Y^{3+} (Dy^{3+}, Eu^{3+}, and Tb^{3+}) ions is surrounded by two nearest AlO$_4$$^{5-}$ (tetrahedral site) and AlO$_6$$^{9-}$(-octahedral site).

4.2 Scanning electron microscopy, SEM mapping, and EDX analysis

The FESEM is a significant technique for detecting surface morphology, crystallite size, EXD mapping, and elemental mapping of the synthesized phosphor samples [50, 53, 57]. Figure 4a–c displays FE-SEM micrographs, elemental mapping, and EDX spectra of the prepared YAG:DyEuTb$_{0.02}$ phosphor. Figure 4a represent irregular morphology, un-equal sizes, and micro-nano crystallites (agglomerated) of synthesized phosphor sample. By the lineal intercept technique [Heyn's, technique or Eq. 6] the average particle size [D_{SEM}] is calculated using the FE-SEM image [64].

$$D_{SEM} = 1.56 \times \frac{L}{MN} \tag{6}$$

Where, M, L, and N is the magnification of images, the length of a line drawn on the images, and grain boundaries intercepted by the lines drawn, respectively. The average crystallite size was calculated to be 50–100 nm for the YAG:DyEuTb$_{0.02}$ sample. Figure 4b, c and Fig. 3S displays an elemental mapping, individual element mapping, and distribution statistics of an elements of the samples. It represents no other elements observe apart from Y, Al, O, Dy, Eu, and Tb. Figure 4c displays EDX spectra of the

Table 3 Rietveld refinement crystallographic data of $Y_3Al_5O_{12}$ and $Y_3Al_5O_{12}$:$Dy_{0.05}Eu_{0.05}Tb_{0.02}$.

Refinement parameters	Refinement values of $Y_3Al_5O_{12}$	Refinement values of $Y_3Al_5O_{12}$:$Dy_{0.05}Eu_{0.05}Tb_{0.02}$
Empirical formula	$Y_3Al_5O_{12}$	$Y_3Al_5O_{12}$
Formula weight	593.62	593.62
Crystal system	Cubic	Cubic
Space group	Ia-3 d	Ia-3 d
Laue class	m-3 m	m-3 m
Unit cell parameters	$a = 12.0069$Å, $b = 12.0069$Å, $c = 12.0069$Å, $\alpha = 90.000°$, $\beta = 90.000°$, $\gamma = 90.000°$	$a = 12.0393$Å, $b = 12.0393$Å, $c = 12.0393$Å, $\alpha = 90.000°$, $\beta = 90.000°$, $\gamma = 90.000°$
Vol	1731.0015 Å^3	1745.0250 Å^3
Calculated density	3.852 g/cm3	4.794 g/cm3
R_p	14.0	12.1
R_{wp}	12.6	10.2
R_{exp}	42.3	8.6
Chi(χ^2)	0.0891	3.7
R_{Bragg}-factor	4.97	9.4
RF-factor	4.33	5.0
D_{W-Stat}	0.0469	0.0954
GoF index	0.30	1.1860
D_{W-exp}	1.8819	1.8819

Table 4 Comparison of refinement crystallographic data for atom parameters of $Y_3Al_5O_{12}$ and $Y_3Al_5O_{12}$:$Dy_{0.05}Eu_{0.05}Tb_{0.02}$.

Atoms	Valence state	Atomic co-ordinate						B_{iso}		Occupancy/sof		Mult.
		x		y		z						
		Host	Doped	Host	doped	Host	Doped	Host	Doped	Host	Doped	
O1	2+	0.032	0.030	0.054	0.039	0.646	0.639	1.498	0.563	5.290	4.296	96
Y1	3+	0.250	0.250	0.125	0.125	0.000	0.000	1.564	1.581	0.963	1.134	24
Al1	3+	0.250	0.250	0.375	0.375	0.000	0.000	0.893	1.099	1.141	1.095	24
Al2	3+	0.000	0.000	0.000	0.000	0.000	0.000	0.461	2.632	0.815	0.907	16

YAG:DyEuTb$_{0.02}$ sample. it represents perfect elemental composition, and homogeneity of the synthesized sample.

4.3 Transmission electron microscopy (TEM) analysis

TEM is a significant technique for observing information about the crystal structure, particle size, pores or voids, defect, particles distribution, selected area electron diffraction (SAED) analysis, and high resolution (HR) analysis of the synthesized sample. In this study, we were observed and collected TEM images of YAG:DyEuTb$_{0.02}$ sample is shown in Fig. 5a–e. Figure 5a & b shows the average crystallite size is found range from 15 to 40 nm, which are like sphere of small nanoparticles, but some agglomerated (100 nm–1 μm) of nanoparticles is observed. The bigger (agglomerated particles) particles having found pores, defect, and dis-similarity due to exothermic reaction of combustion [53, 57–61].

The ImageJ software is used to estimate the size of particle of TEM image (Fig. 5a & b) in which about 100 particle is considered for plotting the graph is shown in Fig. 5c. The histogram is fitted with the log-normal distribution curve (blue line), the mean particle size of around 15 nm is observed, which matches with the results obtained from the XRD measurement. Figure 5d shows SAED (selected area
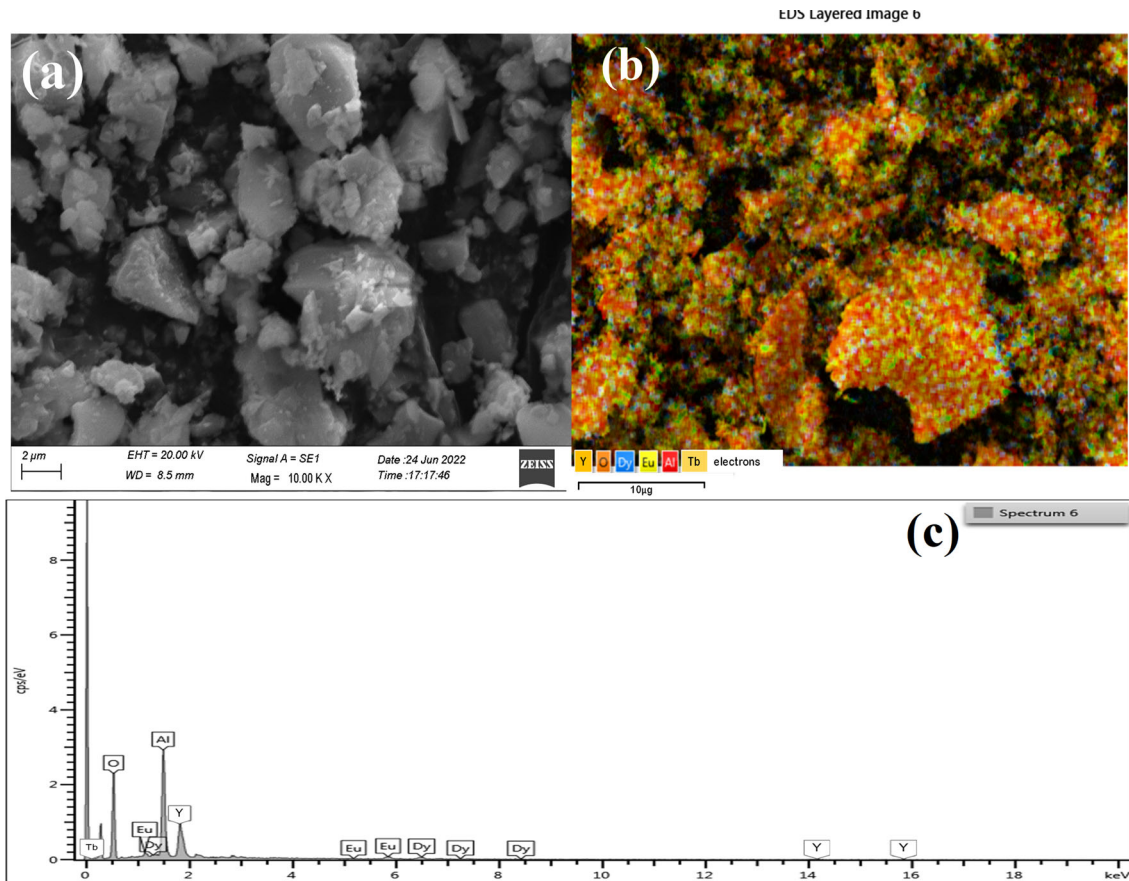
Fig. 4 a–c Typical FESEM surface morphology, energy dispersive X-ray mapping of elements, energy dispersive X-ray (EDX) spectra of YAG:DyEuTb$_{0.02}$.

of electron diffraction) pattern of the sample in which 10 diffraction circular rings are observed at 1st [211], 2nd [220], 3rd [231], 4th [440], 5th [420], 6th [422], 7th [532], 8th [444], 9th [640], and 10th [642] is shown in Fig. 5d. Figure 5e displays a HR-TEM (High Resolution) image of sample in which HR lattice fringes are occupied at different location of image. The interspacing distance between two lattice fringes is measured at different location it varies from 0.504 to 0.824 nm. The measured interspacing distance is perfectly equivalent to the interplanar spacing (*d*) which is calculated by Bragg equation. Therefore, the SAED pattern and HR image of sample is perfectly verify result of PXRD patterns of YAG:DyEuTb$_{0.02}$ samples.

4.4 FTIR analysis

The FTIR spectra displays bands from 550 to 4000 cm^{-1} for YAG:DyEuTb$_{0.02}$ sample is shown in Fig. 6. The FTIR bands located at $\sim$ 786 cm^{-1} and $\sim$ 687 cm^{-1} indicates the vibration of Al–O, while the bands at $\sim$ 721 cm^{-1} and $\sim$ 568 cm^{-1} is observed due to Y–O groups, the separation and sharpness peaks of Y–O and Al–O indicates perfect crystalline structure YAG:DyEuTb$_{0.02}$ [7]. In the spectra, there is does not found any impurity of organic and in-organic elements. Therefore, intensity of emission enhanced by reducing non-radiative relaxations.

4.5 Raman analysis

The Raman spectroscopy is an important technique for detecting the frequency of long-wavelength of lattice vibrations of phonons as well as useful for detecting of grain size, disorders of crystals, impurity level, impurity, crystal structure, residual stress, and defect of crystal symmetry [53]. The Raman spectra of YAG:DyEuTb$_{0.02}$ sample were observed at room temperature which displayed in Fig. 7. In this spectra, 6 peaks were recorded at $\sim$ 139 cm^{-1}, $\sim$ 867 cm^{-1}, $\sim$ 914 cm^{-1}, $\sim$ 1358 cm^{-1}, $\sim$ 1391 cm^{-1}, and $\sim$ 1579 cm^{-1}. The sharp and

Fig. 5 **a**, **b** The photograph of TEM images for the YAG:DyEuTb$_{0.02}$, **c** typical histogram plot indicates distribution of nanoparticles, **d** Typical SAED image for YAG:DyEuTb$_{0.02}$ and **e** HR image for YAG:DyEuTb$_{0.02}$ sample

spectra evidence of good fluorescence properties of samples [53].

4.6 Photo-luminescence analysis

4.6.1 Photo-luminescence analysis of YAG:Dy

Photoluminescence (PL) is a significant characterization technique for characterize the optoelectronic properties of phosphors and semiconductor
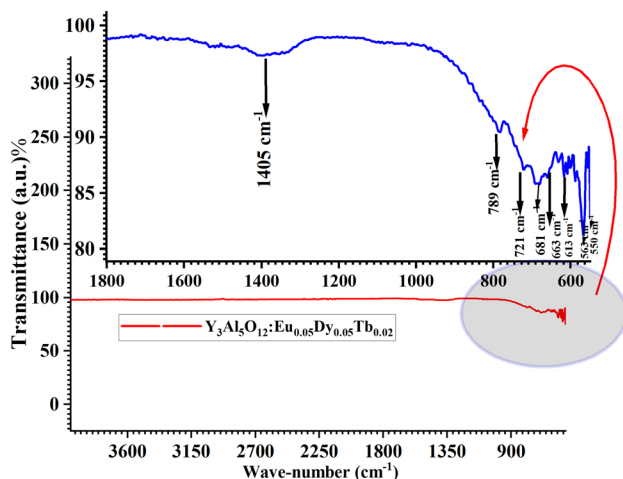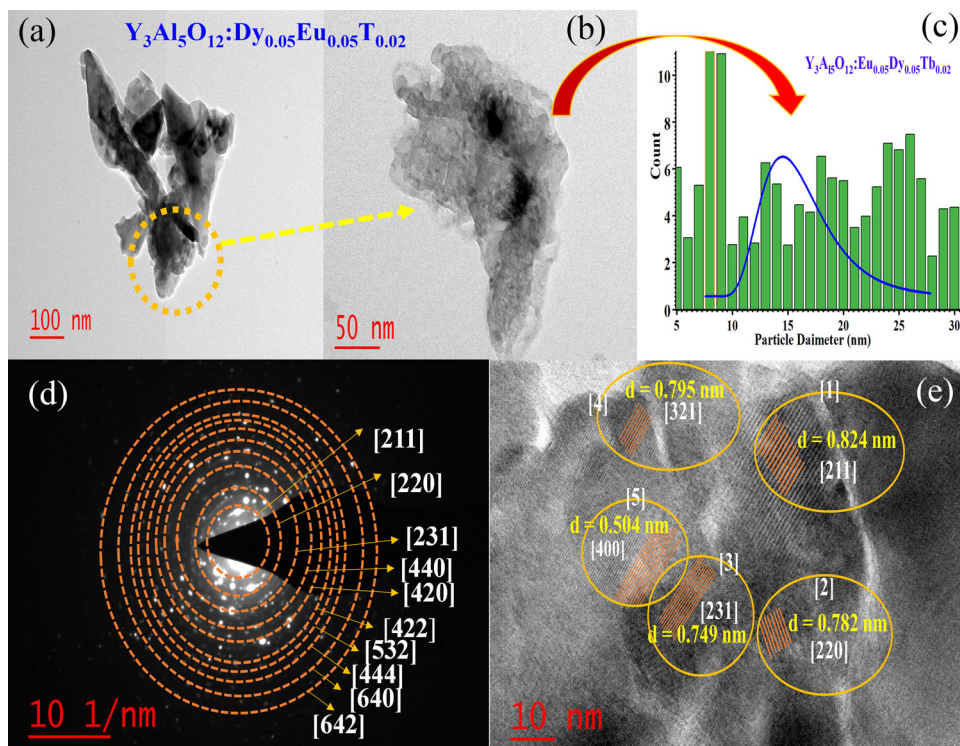

Fig. 6 Typical FT-IR spectra of the YAG:DyEuTb$_{0.02}$ and inset plot represents zooming area of YAG:DyEuTb$_{0.02}$ sample

highest peak has found at ~ 1391 cm^{-1}, which exhibits maximum crystalline crystal symmetry of synthesized YAG:DyEuTb$_{0.02}$ sample. Some other peaks of Raman spectra indicate the cubic spinel anti-symmetry or asymmetric bending vibration of YAG:DyEuTb$_{0.02}$ due to the vibrations, oscillation, and scattering phenomenon of multiple optical phonons. Sharpness and intensive bands of Raman
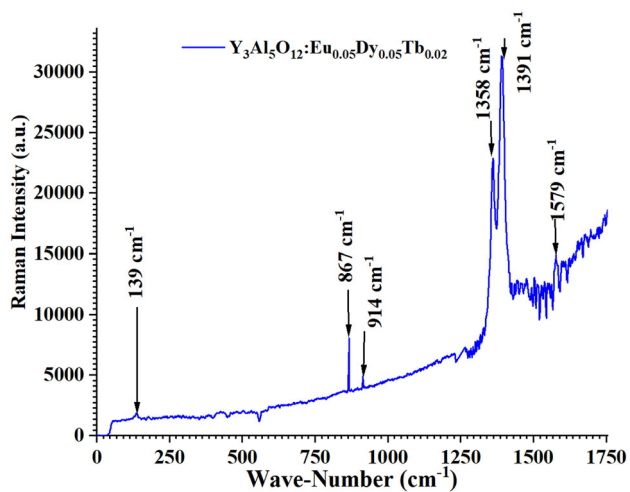

Fig. 7 Typical Raman spectra of the YAG:DyEuTb$_{0.02}$ sample

materials. Its principle is electrons are excited from the ground state to the conductance state of the material by a Xenon laser source with an energy larger than the bandgap. PL is the important phenomenal for the solid-state lighting application. In this work various phosphor sample were synthesized by combustion synthesis route, synthesized sample are listed in Table 1. Before this work several researchers have been synthesized YAG based phosphor doped with Dy rare earth metals by various method. After intense review of research papers, we were synthesized YAG based phosphor doped with Dy, Eu, and Tb rare earth metals.

Figure 8 displays the PL excitation (λ_{em} = 482 nm) and PL emission (λ_{em} = 350 nm) spectra, of $Y_3Al_5O_{12}$:$Dy_{0.05}$ (YAG:Dy) phosphor. In the PL excitation spectra has several excitation peak is originated at around 290 nm (charge transfer), 328 nm ($^6H_{15/2} \rightarrow$ $^4M_{21/2}$), 354 nm ($^6H_{15/2} \rightarrow$ $^4P_{7/2}$), 369 nm ($^6H_{15/2} \rightarrow$ $^4P_{5/2}$), 390 nm ($^6H_{15/2} \rightarrow$ $^4I_{13/2}$), 430 nm ($^6H_{15/2} \rightarrow$ $^4G_{11/2}$), 455 nm ($^6H_{15/2} \rightarrow$ $^4I_{15/2}$), and 476 nm ($^6H_{15/2}$ $\rightarrow$ $^4F_{9/2}$). The weak band originates due to charge transfer phenomenon and sharp excitation bands originates at lower frequency region due to the f-f transitions of Dy^{3+}ions [40, 53, 65, 66].

In the PL emission spectra has two emission peaks is originated at around 482 nm ($^4F_{9/2} \rightarrow$ $^6H_{15/2}$) and 577 nm ($^4F_{9/2} \rightarrow$ $^6H_{13/2}$) due to magnetic dipole transition and electric dipole transitions of Dy^{3+} ions, respectively. It is noticed that 482 nm (blue emission) peak is more dominant to the 577 nm (yellow emission) peak due high local symmetry site of Dy^{3+} in the crystal structure [66]. It is observed that the values of Y/B ratio for various concentration is 0.8074.
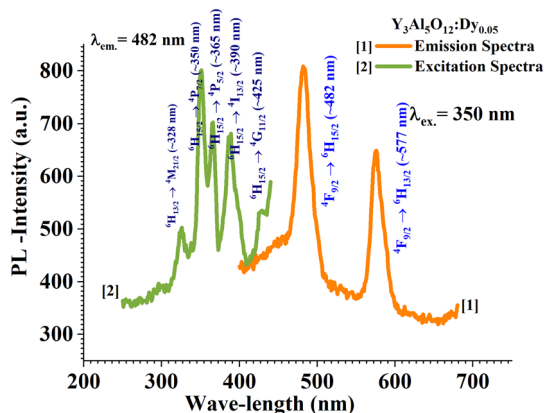

Fig. 8 Typical PL excitation spectra and emission spectra for YAG:Dy

Before this work, application of Dy doped various phosphors as a WLEDs application have been already reported by researchers, because they were obtained a ratio of yellow and blue peaks of emission spectra (Y/B) to one or more by appropriate doping of a single Dy^{3+} in many such suggested host compounds and adjusting the ratio of the peaks in the blue and yellow regions [1]. Thus, it is possible to obtain white light in a single Dy^{3+} doped phosphor material by appropriately adjusting the yellow to blue intensity ratio (Y/B). But if the ratio of yellow color and blue color remains one or less then this type of phosphor material is not suitable for making WLEDs. therefore, research is unmoving required to achieve high quality white light with high emission intensity, after the co-doping of Eu and Tb (red and green emitting component) with suitable concentration of Dy^{3+}, that high white light can be generated.

The Y/B ratio of Dy^{3+} is related to many factors, co-doping of another sensitizer which due to enhance the intensity of yellow peak, the site symmetry of activators, and electronegativity of the next-neighbor element [66]. In this research work we were used to co-doping of Eu and Tb ions for enhancing the intensity of yellow peak, improve quantum efficiency, increase value of CRI, and enhancing color purity of emitting white color. Therefore, in this work we have taken Eu rare earth elements as a red component and Tb elements as a green components of PL spectra. The decay curve, CIE color co-ordinate, CRI, CCT, and quantum efficiency is calculated of YAG:Dy phosphor sample all values is shown in following Table 1S, Tables 5 and 6. From the analysis of all-result, prepared YAG:Dy sample is not suitable for WLEDs white lighting system.

4.6.2 Photo-luminescence analysis of YAG:Eu

The PL excitation spectra of YAG:Eu phosphor was observed by monitoring emission wavelength at 594 nm is shown in Fig. 9. The characteristic lines located at 322 nm ($^5L_6 \rightarrow^7F_0$), 330 nm ($^5L_6 \rightarrow^7F_1$), 364 nm ($^5L_6 \rightarrow^7F_2$), 386 nm ($^5L_6 \rightarrow^7F_3$), 394 nm ($^5L_6 \rightarrow^7F_4$), 408 nm ($^5D_2 \rightarrow^7F_0$), 467 nm ($^5D_2 \rightarrow^7F_1$), and 477 nm ($^5D_2 \rightarrow^7F_2$) are attributed due to transitions of Eu^{3+} ions [65, 66].

The PL emission spectra YAG:Eu was observed by under the monitoring of excitation wavelength 394 nm, the PL emission spectra exhibits emission bands at 591 nm ($^5D_0 \rightarrow^7F_1$), 594 nm ($^5D_0 \rightarrow^7F_1$), and

Table 5 Listed sample code, CIE color coordinate, color purity, CRI, and CCT and critical distance values of phosphors sample

Sample code	CIE color co-ordinate (X, Y)	Dominant CIE color co-ordinate (X_d, Y_d)	Color purity (%)	CRI	CCT (K)
YAG:Dy	(0.3083, 0.3170)	(0.275, 0.05)	91	90	6871
YAG:Eu	(0.3927, 0.2990)	(0.569, 0.05)	81	57	2821
YAG:Tb	(0.3289, 0.3592)	(0.277, 0.713)	92.44	96	5252
YAG:DyEu	(0.3257, 0.3049)	(0.280, 0.052)	90.98	90	5892
YAG:DyEuT$_{0.01}$	(0.3418, 0.3286)	(0.479, 0.147)	97.03	93	5057
YAG:DyEuT$_{0.02}$	(0.3369, 0.3312)	(0.562, 0.182)	95.68	95	5287
YAG:DyEuT$_{0.03}$	(0.3405, 0.3285)	(0.562, 0.182)	96.145	93	5117
YAG:DyEuT$_{0.04}$	(0.3444, 0.3301)	(0.718, 0.28)	96.319	93	4947

Table 6 Calculated internal and external, and quantum efficiency (QE) of the phosphor materials

Sample name	EQE (%)	IQE (%)	QE(%)
YAG:Dy	85.4	93.1	94.9
YAG:Eu	82.6	93.7	92.2
YAG:Tb	84.9	93.6	94.3
YAG:DyEu	86.1	93.5	94.1
YAG:DyEuTb$_{0.01}$	82.7	92.7	93.6
YAG:DyEuTb$_{0.02}$	85.1	93.1	93.7
YAG:DyEuTb$_{0.03}$	85.0	92.5	93.6
YAG:DyEuTb$_{0.04}$	84.7	92.7	93.4

599 nm ($^5D_0 \rightarrow {}^7F_1$) magnetic dipole transition, But the PL emission spectra exhibits emission bands at ~ 612 nm ($^5D_0 \rightarrow {}^7F_2$), ~ 630 nm ($^5D_0 \rightarrow {}^7F_2$), ~ 650 nm ($^5D_0 \rightarrow {}^7F_3$), and ~ 708 nm ($^5D_0 \rightarrow {}^7F_4$) due to the electric dipole transition, respectively is shown
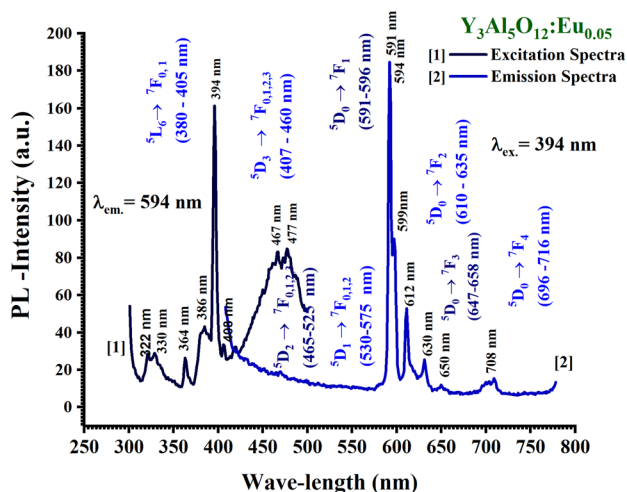

Fig. 9 Typical PL excitation spectra and emission spectra for YAG:Eu

in Fig. 9. In this study, the magnetic dipole transition is stronger than the electric dipole transitions, it indicates that these Eu^{3+} ions occupy strong symmetry sites of crystal [66]. The decay curve, CIE color co-ordinate, CRI, CCT, and quantum efficiency is calculated of $Y_3Al_5O_{12}$: $Eu_{0.05}$ phosphor sample all values is shown in following Table 1S, Tables 5 and 6. It is concluded that the prepared YAG:Eu phosphor material is suitable for red lighting system.

4.6.3 Photo-luminescence analysis of YAG:Tb

Figure 10 displays the PL excitation spectra of YAG:Tb phosphors and it was monitored under the an emission wavelength 547 nm and slit width 1.5 nm. The characteristic lines located at ~ 329 nm ($4f_8 \rightarrow 4f_7 5d_1$ transition of Tb^{3+}). Meanwhile, the strong excitation band at ~ 307 and 315 nm which was attributed due to the $^8S_{7/2} \rightarrow {}^6P_{7/2}$ and $^8S_{7/2} \rightarrow {}^6P_{3/2}$, respectively, three more other strong band were found at ~ 353 nm ($^7F_6 \rightarrow {}^5L_9$), ~ 378 nm ($^7F_6 \rightarrow {}^5G_9$), and ~ 397 nm ($^7F_6 \rightarrow {}^5L_{10}$) have been found of transition Tb^{3+} [67]. The PL emission spectra were

Table 7 PL Main intensity for one of the peaks, average life time decay, logarithmic values of average life time and energy transfer efficiency of the synthesized phosphor samples

Samples	Main Intensity	Conc. (C)	τ_{av}	η_τ (%)	η_i (%)	Log(τ_{av})
YAG:Eu	814 (I_0)	0.05	2.162944			
YAG:Dy	186	0.05	1.599267			
YAG:Tb	997	0.02	2.621224			
YAG:DyEu	**526** (Is)	**0.1**	2.252535	41.1221516	35.3808	− 0.1485
YAG:DyEuTb$_{0.01}$	403 (Is)	0.11	2.396777	49.8672204	50.4914	− 0.17570
YAG:DyEuTb$_{0.02}$	**412** (Is)	**0.12**	2.402394	50.2184438	49.3857	− 0.17672
YAG:DyEuTb$_{0.03}$	401 (Is)	0.13	2.419566	51.2922159	50.7371	− 0.17981
YAG:DyEuTb$_{0.04}$	398 (Is)	0.14	2.434601	52.2323343	51.1057	− 0.18250

Table 8 PL intensity's, relative PL intensity's, PL intensity with respect to concentrations, concentration of activators and sensitizer with activators, logarithmic values concentration of activator and sensitizers of phosphors samples

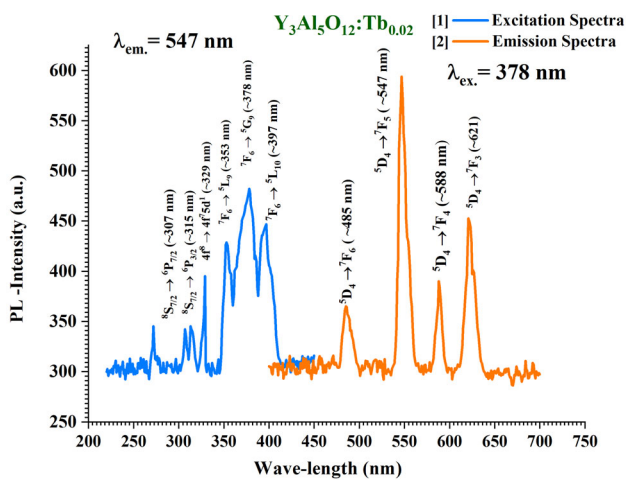| Intensity (I_s)	I_0/Is	Cont.	$(C)^{n/3}$, ($n = 6$)	$(C)^{n/3}$, ($n = 8$)	$(C)^{n/3}$, ($n = 10$)	Log(I_0/I_s)	Log(c)	Log(I/c)
526	1.547529	**0.10**	0.0100	0.00215	0.000464	0.1896	− 1	3.72098
403	2.019851	0.11	0.0121	0.00270	0.000637	0.305319	− 0.958	3.56391
412	1.975728	**0.12**	0.0144	0.00350	0.000852	0.295727	− 0.920	3.53571
401	2.029925	0.13	0.0169	0.00433	0.001112	0.307480	− 0.886	3.48920
398	2.045226	0.14	0.0196	0.00528	0.001424	0.310741	− 0.853	3.4537

Fig. 10 Typical PL excitation spectra and emission spectra for YAG:Tb compound

$Y_3Al_5O_{12}$: Tb^{3+} phosphors characteristic bands located at ∼ 485 nm ($^5D_4 \rightarrow {}^7F_6$), ∼ 547 nm ($^5D_4 \rightarrow {}^7F_5$), ∼ 588 nm ($^5D_4 \rightarrow {}^7F_4$), and ∼ 621 nm ($^5D_4 \rightarrow {}^7F_3$) which due to transitions (electric dipole and magnetic dipole induced) of Tb^{3+} [67]. The YAG:Tb^{3+} phosphor emits green band (∼ 547 nm) is stronger than other bands. Additionally, high intensity bands have been observed for Tb^{3+} (< 272 nm) due to Tb-O charge transfer band [67]. The decay curve, CIE color co-ordinate, CRI, CCT, and quantum efficiency is calculated of $Y_3Al_5O_{12}$:$Tb_{0.02}$ phosphor sample all values is shown in following Table 1S, Tables 5 and 6. From the analysis of YAG:Tb phosphor, it can be suitable for green lighting system.

4.6.4 Photo-luminescence analysis of YAG:DyEu

The PL excitation spectra of YAG:DyEu phosphor was monitored under an emission wavelength 614 nm is shown in Fig. 11. The characteristic lines
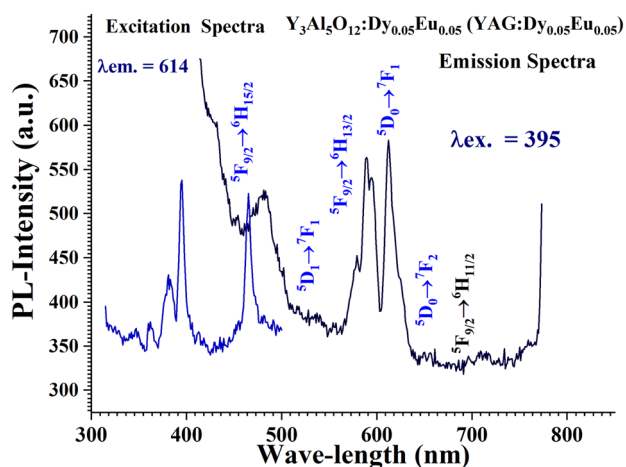
observed of the $Y_3Al_5O_{12}$: Tb^{3+} phosphor under the monitoring of an excitation wavelength of 378 nm is shown in Fig. 10. The PL emission spectra of

Fig. 11 Typical PL excitation spectra and emission spectra for YAG:DyEu.

located at ∼ 346 nm ($^6H_{15/2} \rightarrow {}^4P_{7/2}$), ∼ 361 nm ($^6H_{15/2} \rightarrow {}^4P_{5/2}$), ∼ 380 nm ($^6H_{15/2} \rightarrow {}^4I_{13/2}$) due to Dy^{3+} and it may some of these characteristic lines located at ∼ 361 nm ($^5L_6 \rightarrow {}^7F_2$), ∼ 380 nm ($^5L_6 \rightarrow {}^7F_3$), ∼ 395 nm ($^5L_6 \rightarrow {}^7F_4$), ∼ 464 nm ($^5D_2 \rightarrow {}^7F_1$) due to Eu^{3+} ions. Therefore, it is observed that the excitation of Dy^{3+} and excitation spectra of Eu^{3+} is overlapping criterion due to energy gets transfer from higher energy level (Dy^{3+}) to lower energy level (Eu^{3+}). Therefore, peak intensity of Dy^{3+} is diminished. The PL emission spectra of YAG:DyEu phosphor was monitored at 395 nm is shown in Fig. 11. The PL characteristic bands is located at ∼ 482 nm ($^4F_{9/2} \rightarrow {}^6H_{15/2}$), ∼ 577 nm ($^4F_{9/2} \rightarrow {}^6H_{13/2}$), ∼ 654 nm ($^4F_{9/2} \rightarrow {}^6H_{11/2}$), ∼ 591 nm ($^5D_0 \rightarrow {}^7F_1$), and ∼ 612 nm ($^5D_0 \rightarrow {}^7F_2$) nm due to the transitions of Dy^{3+} and Eu^{3+}ions [66]. In the PL emission spectra displays two characteristic lines at 482 and 577 nm is observed due to Dy^{3+} transition, and two another characteristic lines at 591 and 614 nm are observed due to Eu^{3+} transition is displayed in Fig. 11.

The PL emission spectra of YAG:DyEu phosphor was monitored at 395 nm is shown in Fig. 11. The PL characteristic emission bands are located at ∼ 480 nm ($^4F_{9/2} \rightarrow {}^6H_{15/2}$), ∼ 575 nm ($^4F_{9/2} \rightarrow {}^6H_{13/2}$), ∼ 656 nm ($^4F_{9/2} \rightarrow {}^6H_{11/2}$) due to the transitions of Dy^{3+} and another PL emission bands is observed at ∼ 537 nm ($^5D_1 \rightarrow {}^7F_1$), ∼ 595 nm ($^5D_0 \rightarrow {}^7F_1$), and ∼ 612 nm ($^5D_0 \rightarrow {}^7F_2$) due to transitions of Eu^{3+}ions [66]. In the PL emission spectra, it is observed that an overlaps band is found between yellow emission (577 nm) of Dy^{3+} ion and orange red emission (591 nm) of Eu^{3+} ions. Therefore, energy get transfer

from Dy^{3+} to Eu^{3+} resultantly, PL emission intensity increases of the Eu^{3+} ($^5D_0 \rightarrow {}^7F_2$) while the PL emission intensity diminishes of Dy^{3+} ($^4F_{9/2} \rightarrow {}^6H_{13/2}$) [66].

4.6.5 Photo-luminescence analysis of YAG:DyEuTb$_{1-x}$

The PL excitation spectra of YAG:DyEuTb$_{1-x}$ (x = 0.01, 0.02, 0.03, and 0.04) were monitored under an emission wavelength 544 nm is shown in Fig. 12. The characteristic bands located at ∼ 277 nm ($4f_8 \rightarrow 4f_7 5d_1$) due to Tb^{3+}, ∼ 350–356 nm [($^6H_{15/2} \rightarrow {}^4P_{7/2}$) doe to Dy^{3+} ions & ($^5L_6 \rightarrow {}^7F_2$) due to Eu^{3+}], ∼ 382 nm [($^5D_3 \rightarrow {}^7F_6$) due to Tb^{3+}, ($^6H_{15/2} \rightarrow {}^4I_{13/2}$) due to Dy^{3+}, and ($^5L_6 \rightarrow {}^7F_3$) due to Eu^{3+}], 450 nm ($^6H_{15/2} \rightarrow {}^4I_{15/2}$) due to Dy^{3+}, ∼ 464 nm ($^5D_2 \rightarrow {}^7F_1$) due to Eu^{3+}, ∼ 477 nm($^6H_{15/2} \rightarrow {}^4F_{9/2}$) due to Dy^{3+}, and ∼ 490 nm ($^5D_4 \rightarrow {}^7F_6$) due to Tb^{3+} ions. The excitation spectra range from 250 to 500 nm several peaks originate by the co-contribution and overlapped transition of Dy^{3+}, Eu^{3+}, and Tb^{3+} ions [66, 67]. The PL emission spectra of YAG:DyEuTb$_{1-x}$ (x = 0.01, 0.02, 0.03, and 0.04) phosphor is observed under the monitoring of an emission wavelength 356 nm is shown in Figs. 4S and 13, & Fig. 5S. The maximum PL intensity is observed for YAG:DyEuTb$_{0.02}$, after increases concentration of Tb PL intensity decrease gradually due to concentration quenching. The cause of concentration quenching phenomena is described below (Figs. 17 and 18). The PL emission characteristic bands located at ∼ 465 nm ($^5D_2 \rightarrow {}^7F_0$) due to Eu^{3+}, ∼ 482 nm ($^4F_{9/2} \rightarrow {}^6H_{15/2}$) due to Dy^{3+}, ∼ 544 nm ($^5D_4 \rightarrow {}^7F_5$) due to Tb^{3+}, ∼ 577 nm ($^4F_{9/2} \rightarrow {}^6H_{13/2}$) due to Dy^{3+}, ∼ 595 nm ($^5D_0 \rightarrow {}^7F_1$) due to Eu^{3+}, ∼ 612 nm ($^5D_0 \rightarrow {}^7F_2$) due to Eu^{3+}, ∼ 650 nm ($^5D_0 \rightarrow {}^7F_3$) due to Eu^{3+}, and ∼ 708 nm ($^5D_0 \rightarrow {}^7F_4$) due to Eu^{3+} ions. Figures 4S and 13 shows that the PL emission intensity of Dy^{3+}, and Tb^{3+} get diminishes (only one peak at ∼ 544 nm slightly increases with respect to Tb concentration, after concentration quenching it decreases gradually) and intensity of Eu^{3+} get enhances with respect to increases concentration of Tb^{3+} ions, it is the evidence of the energy getting transfer from Tb^{3+} to Eu^{3+} ions.

It is observed that several overlap spectrums are found between blue, yellow, orange, and red PL emission, it indicates the energy transfer takes place from Dy^{3+} to Tb^{3+} and Tb^{3+} to Eu^{3+}. The PL emission intensity increases of the Eu^{3+} ($^5D_0 \rightarrow {}^7F_2$), while the
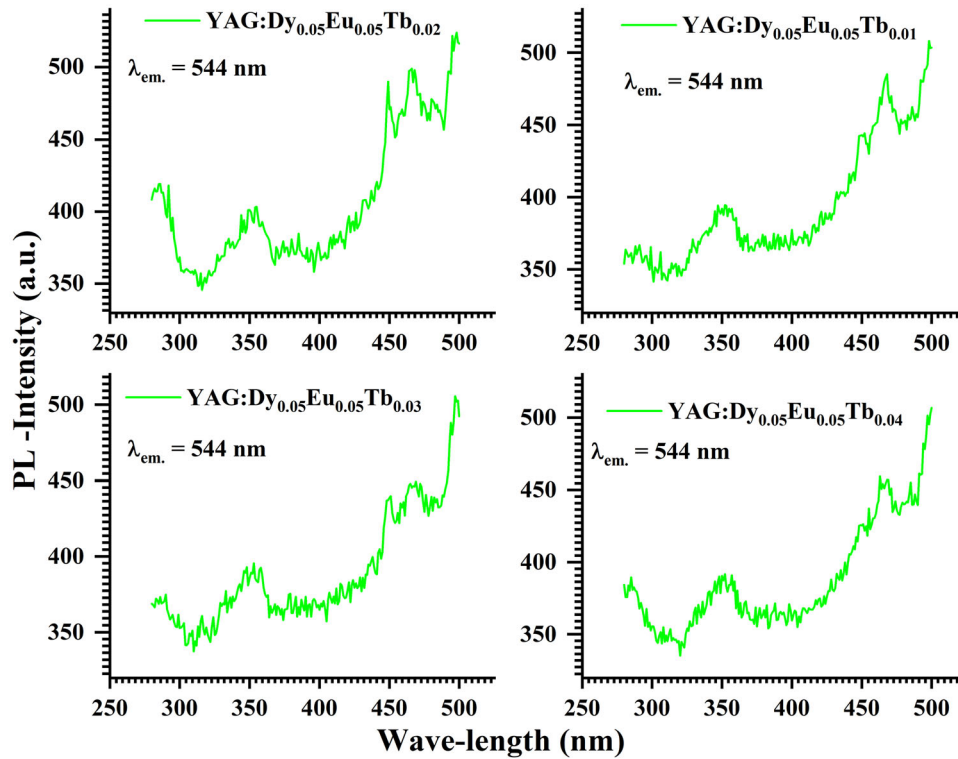
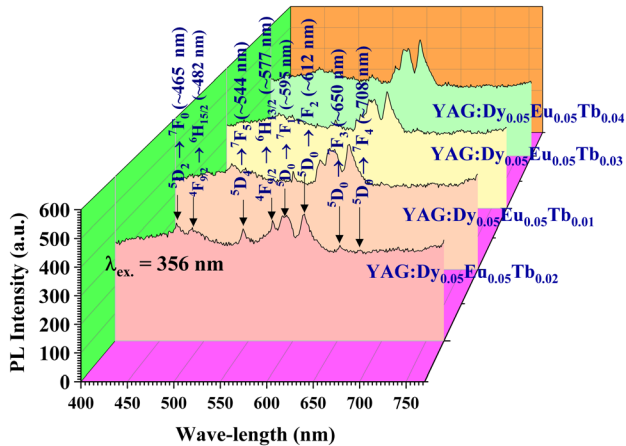**Fig. 12** Typical PL excitation spectra for YAG:DyEuTb$_{(1-x)}$ (x = 0.01–0.04)

**Fig. 13** Typical PL emission spectra for YAG:DyEuTb$_{(1-x)}$(x = 0.01–0.04)

PL emission intensity diminishes of the Dy^{3+}(^{4}F$_{9/2}$→ ^{6}H$_{13/2}$), and PL emission intensity diminishes of Tb^{3+}(^{5}D$_4$ → ^{7}F$_5$) are shown in Figs. 8, 9 and 10, & 11. These result show that the spectra get clear tuned from blue/yellow to orange/red emission for white light emission.

4.7 PL decay analysis

Figures 14 and 15 displays the decay curves were recorded of various samples such as YAG:Dy, YAG:Eu, YAG:Tb, YAG:Dy, Eu, and YAG:DyEuTb$_{1-x}$ (x = 0.01, 0.02, 0.03, and 0.04). PL spectra were measured under the monitoring of an excitation and an emission wavelength and those same wavelengths are used for measurement of PL decay. For the determination of fitting parameters double-exponential decay function is used according to Eq. (7) [57, 68]. Where, $I(t)$ is the PL intensity t is the time, A$_1$ & A$_2$ is the fitting constants, τ_1 is the short life time decay, τ_2 is the long life time decay. The average lifetime τ_{av} has been calculated by Eq. (8) and average life time is listed in Table 7 [68].

Based on the above Eq. (7), the luminescence lifetimes of samples have determined of all samples, short- and long-life time decay time and fitting constant are listed in Table 1S. YAG based phosphors activated with rare earth metals gives efficient life time decay with respect to concentration of Eu and Tb. The decay curve exhibits are enhanced life time decay. The YAG:DyEuTb$_{0.02}$ sample has exhibited more take persistence time with respect to other

Fig. 14 Typical photoluminescencedecay result for YAG:Dy, YAG:Eu, YAG:Tb, and YAG:Dy,Eu samples
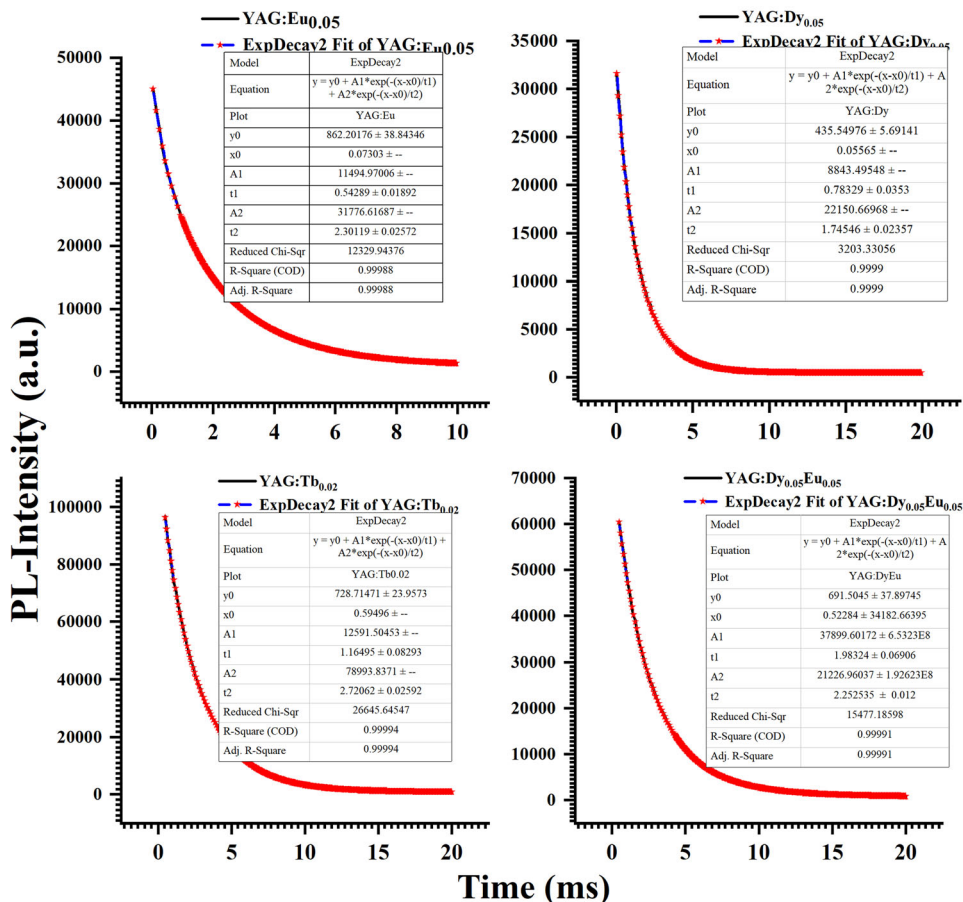
samples due to after increasing concentration of Tb and PL intensity were decreased as shown in Table 1S.

$$I(t) = A_1 exp\left(-\frac{t}{\tau_1}\right) + A_2 exp\left(-\frac{t}{\tau_2}\right) \quad (7)$$

$$\tau_{av} = \frac{A_1\tau_{1+}^2 A_2\tau_2^2}{A_1\tau_1 + A_2\tau_2} \quad (8)$$

4.8 Critical distance

we have calculated relative distance or critical distance by the Blasse's Eq. (9) [4, 39, 57] for YAG:DyEuTb$_{0.02}$ sample.

$$R_0 = 2\left[\frac{3V}{4\pi X_C N}\right]^{1/3} \quad (9)$$

Where V = 17450.25 volume of unit cell, Xc = 0.12, critical concentration of Eu, Dy, and Tb, N = 8, is the number cation per unit YAG cell. The R_o was Calculated to be about 15.1397 Å. Thus, calculated value of R_o is greater than 5Å. Therefore, it indicates that

possibility of energy transfer by exchange interaction mechanism between Dy^{3+}, Eu^{3+}, and Tb^{3+} ions.

4.9 Energy transfer efficiency

The energy transfer efficiencies are calculated as a function of Eu^{3+}/Tb^{3+} sensitizer concentration under 356 excitations. In this work the energy transfer efficiency (η) is calculated using by two methods Eqs. (10) & (11) [4, 69–71]. First, by using PL intensity of YAG based activator (Dy), and PL intensity of YAG based activator with sensitizer (Eu and Tb), and second by using average life time decay for YAG based activator and activator with sensitizer. The PL emission intensity of samples and calculated energy transfer efficiency are tabulated in Table 7.

$$\eta_{ET} = \left[1 - \frac{I_{Dy}}{I_{Dy} + I_{Eu} + I_{Tb}}\right] \quad (10)$$

Where, $I_{Dy} = I_{S0}$, $I_S = I_{Dy} + I_{Eu} + I_{Tb}$, and I_{S0} is the PL intensity of YAG:Dy$_{0.05}$ (absence of a sensitizer), I_s the PL intensity of YAG:DyEuTb$_{1-x}$ [the presence of a
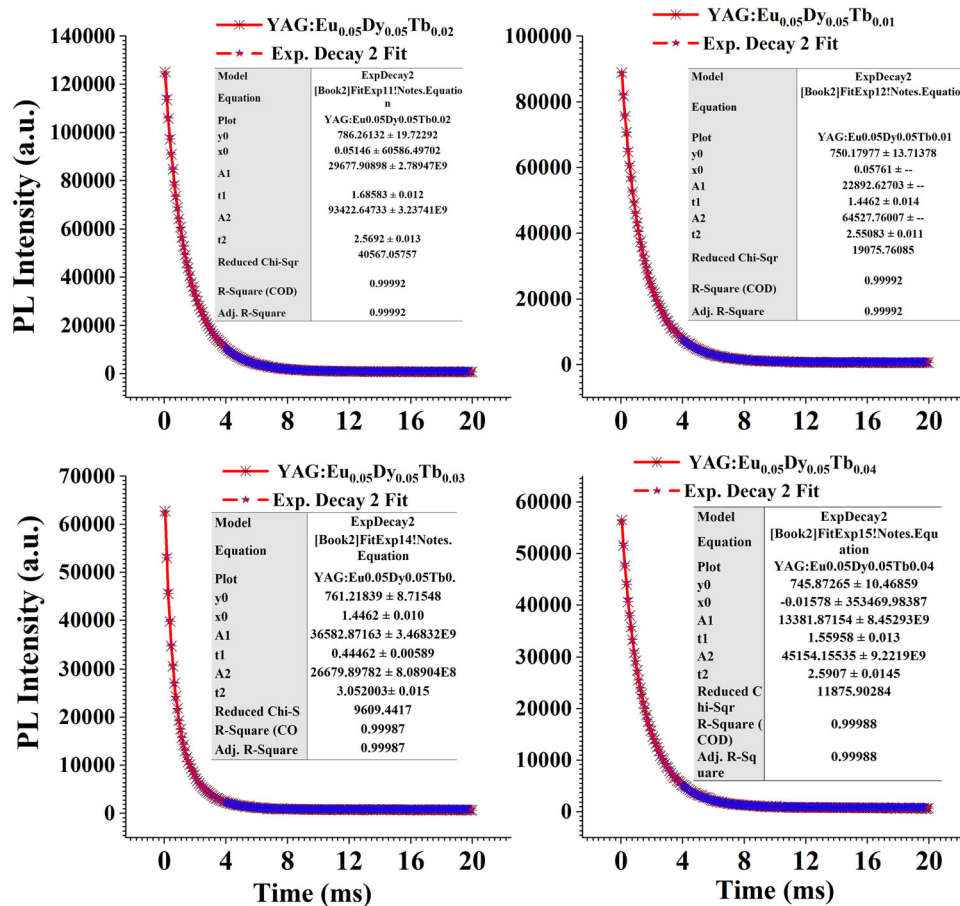
Fig. 15 Typicalphotoluminescence decay result for YAG:DyEuTb$_{(1-x)}$ (x = 0.01, 0.02,0.03, and 0.04 mol)

sensitizer (Eu^{3+} and Tb^{3+})], where x is varied from 1 to 4 mol%.

Again, we have calculated the energy transfer efficiency by using average decay time for activator and activator with sensitizer using Eq. (11), where τ_s and τ_{s0} are the photo-luminescence average lifetime decay of the activator (Dy^{3+}) and activator with sensitizer ions (Dy^{3+}/Eu^{3+}/Tb^{3+}), respectively.

$$\eta_{ET} = \left[1 - \frac{\tau_{Dy}}{\tau_{Dy} + \tau_{Eu} + \tau_{Tb}}\right] \tag{11}$$

Where $\tau_{Dy} = \tau_{S0,}, \tau_S = \tau_{Dy} + \tau_{Eu} + \tau_{Tb}$, τ_{Dy} is the average decay time for YAG:Dy and τ_s is the average time decay for YAG:DyEuTb(1−x). From Fig. 15 and the calculated result is tabulated in Table 7. The energy transfer efficiency for YAG:Dy^{3+}-Eu^{3+}-Tb^{3+} can reach maximum around ∼ 51% and its depends on concentration of sensitizer. This calculated efficiency of energy transfer is estimated by non-radiative transition. We have observed the energy transfer efficiencies by both methods approximately are

found same result, that calculated result indicates energy transfer from Dy^{3+} to Tb^{3+} and Tb^{3+} to Eu^{3+}.

4.10 Energy transfer mechanism

In this section we are studied Energy transfer mechanism only for YAG:DyEuTb$_{1-x}$ (x = 0.01, 0.02, 0.03, and 0.04) sample, previously several researchers have been reported for energy transfer mechanism for various rare earth ions and pare of rare earth ions [4–25]. The energy level of Eu^{3+} is a little lower than that of Tb^{3+}, therefore, energy transfer through due to nonradiative processes occurs from Tb^{3+} ions to Eu^{3+}. On the other hand, the energy level of Dy^{3+} ions higher then Tb^{3+} and Eu^{3+} ions therefore, when the 4f higher energy level of Dy^{3+} is excited then energy transfer to the ^{5}D$_4$ level of Tb^{3+} due to resonance between the two energy levels. The phonon-assisted energy transfer enhances the population of ^{5}D$_4$ levels of Tb^{3+}. Thus, the energy transfers from firstly excited ions Dy^{3+} to Tb^{3+} and then Tb^{3+} to

Fig. 16 Typical Photoluminescence decay result for YAG:Dy, YAG:Eu, YAG:Tb, and YAG:Dy,Eu samples
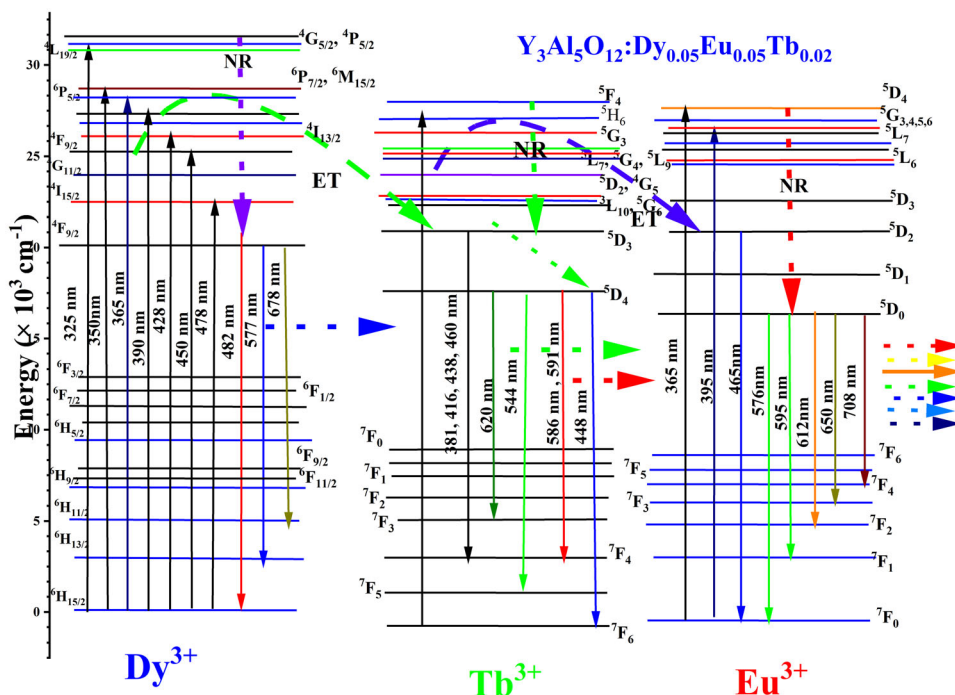
Eu^{3+}, the schematic energy level diagrams of Dy^{3+}, Tb^{3+}, and Eu^{3+} ions for obtaining white light emission are shown in Fig. 16.

The PL emission spectra of YAG:DyEuTb$_{0.02}$ sample were monitored under the excitation of 356 nm. it is observed that Dy^{3+} emissions partly overlap with the excitation wavelengths of Tb^{3+} and Eu^{3+}. After the superpositions of each excitation and emission wavelength of each ions (Dy^{3+}, Eu^{3+}, and Tb^{3+}) reveals that complete PL spectra of the sample. During emission of PL spectra, some transition occurs of the Dy^{3+} ions at $\sim$ 482 nm ($^4F_{9/2} \rightarrow {}^6H_{15/2}$), $\sim$ 577 nm ($^4F_{9/2} \rightarrow {}^6H_{13/2}$), and $\sim$ 612 nm ($^4F_{9/2} \rightarrow {}^6H_{11/2}$). But around 50% energy shift towards the Tb^{3+} and Eu^{3+} ions due to non-radiative process. The Tb^{3+} gives transition due to $^5D_4 \rightarrow {}^7F_5$ ($\sim$ 547 nm) while, Eu^{3+} gives transition due to $^5D_0 \rightarrow {}^7F_1$ (594 nm) and $^5D_0 \rightarrow {}^7F_2$ (612 nm). After the combining all weak and strong transition for emission gives one advance complete white spectra of the proposed sample for WLEDs application.

Types of the interaction energy transfer mechanism according to Inohuti-Hirayama (*I–H* model) and Reisfeld approximation is shown in Eq. (12), [39, 71] where, I_{S0} is the PL intensity of YAG:Dy (absence of a sensitizer), I_s the PL intensity of YAG:DyEuTb$_{1-x}$, (x = 1–4 mol%), and C is the total concentration of doping elements. The I_{so}/I_s versus C$^{n/3}$ plots are

shown in Fig. 17a, b, & c and values are listed in Table 8. The relation is observed when using n = 6, 8, and 10. The highest R^2 values of the linear fittings occurs when n = 6, corresponding to their best linear fitting.

Again, *I–H* model and Reisfeld approximation is shown in Eq. (13) [72, 73], where, C is the total concentration of doping elements, τ_{so} average life time decay for YAG:Dy, and τ_S is the average life time decay of YAG:DyEuTb$_{1-x}$. The τ_{so}/τ_s versus C$^{n/3}$ plots are shown in Fig. 17d, e, & f and measured values are listed in Table 8. The highest R^2 values of the linear fittings occur when n = 6, corresponding to their best linear fitting. Here, both approximations have given same result, therefore, quenching phenomenon and energy transformation process occurs due to dipole-dipole interaction mechanism.

$$\frac{I_{S0}}{I_S} \propto c^{n/3} \tag{12}$$

$$\frac{\tau_{S0}}{\tau_S} \propto c^{n/3} \tag{13}$$

Another theory of energy transfer process of intermolecular exchange (Dexter's energy-transfer and Reisfeld's approximation) expressions of multipolar interaction is calculated by Eq. (14) [74]. Where, n = 6 (dipole–dipole interactions), n = 8 (dipole–quadrupole interactions), and n = 10 (quadrupole–
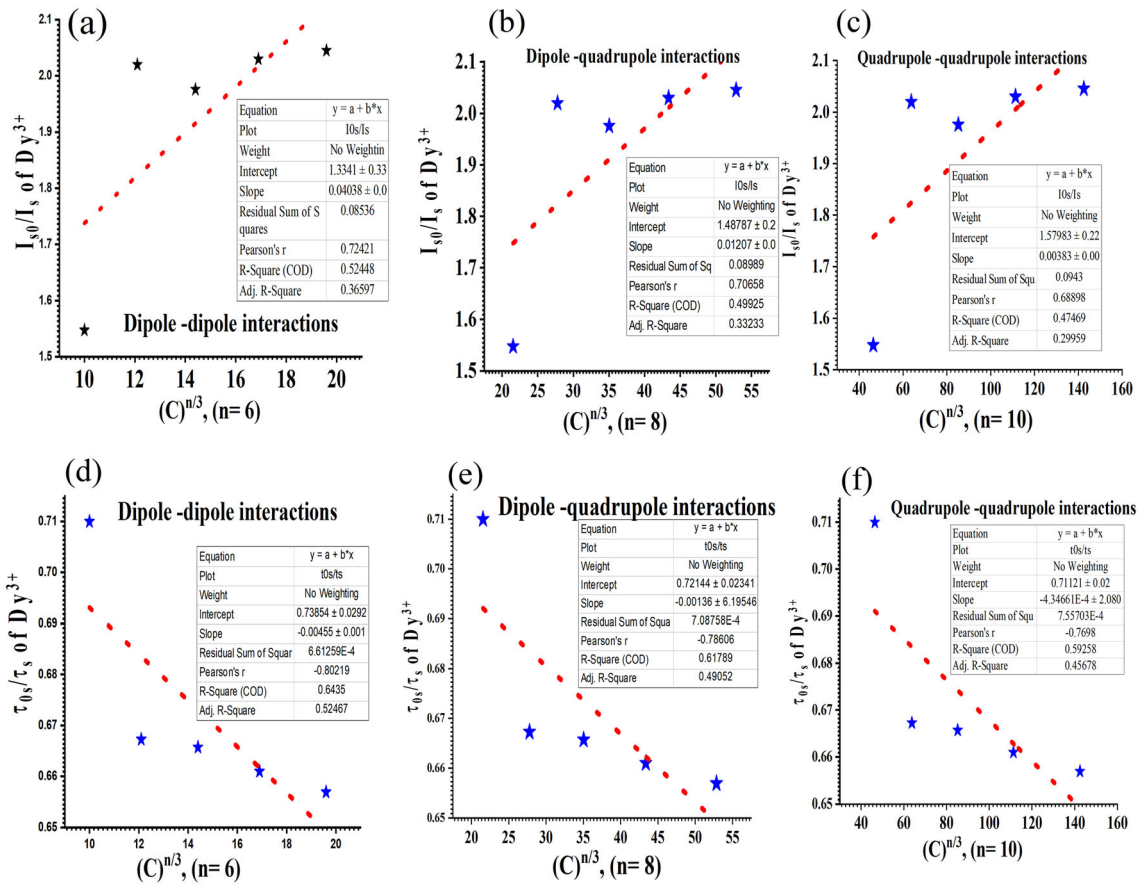
Fig. 17 Typical Photoluminescence decay result for YAG:DyEuTb$_{(1-x)}$ (x = 0.01, 0.02, 0.03, and 0.04 mol)

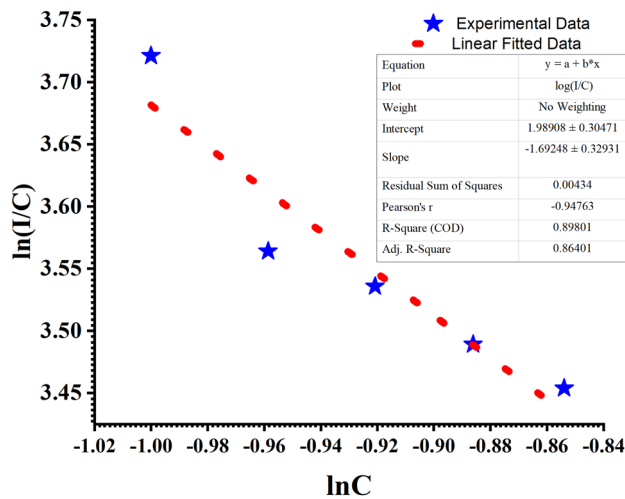**Fig. 18** Typical energy transfer mechanism for YAG:DyEuTb$_{1-x}$ (x = 0.01, 0.02, 0.03, and 0.04 mol) phosphor

quadrupole interactions), C is the doping concentration of the Dy, Eu, and Tb ions. The ln(I/C) versus ln$C$ plots are further illustrated in Fig. 18. where, ln$x$ = ln$K$–lnβ, k and β are constants, I is the PL intensity of YAG:DyEuTb$_{1-x}$ (x = 0.01, 0.02, 0.03, and 0.04).

$$I/C = K\left[\beta C^{Q/3}\right]^{-1}$$

$$\ln\left(\frac{I}{C}\right) = \ln x - (Q/3)\ln C \tag{14}$$

Linear equation of one dimension is $Y = mx + c$, where, M is the slope, by the graph we have observed $M = -1.69248$, therefore, after comparison, $-Q/3 = -1.69248$. The value of $Q = 5.0784$ is close to the 6, therefore, in the present case the main cause of concentration quenching is due to dipole- dipole interaction. The energy transfer parameter (intermolecular exchange interaction) is calculated by Eq. (15) [70].

$$Q = \frac{4\pi}{3}\Gamma\left[1 - \frac{3}{s}\right]C_A R_0^{3/s} \tag{15}$$

Here, Q (Q = 2.02059) depends (energy transfer parameter) on the concentration of acceptors C_A (Eu^{3+} and Tb^{3+}) and types of interaction (dominant

value of $s = 6$), R_o is the critical transfer distance between donor acceptors ions, Γx is the gamma function. The energy transfer parameters increase with increasing the concentration of Tb concentrations.

4.11 CIE chromaticity analysis

International Commission on Illumination or CIE color co-ordinate, CCT, and CRI are most useful parameters for lighting application of the phosphors. In this work, YAG based phosphor synthesized with different doping concentration of Dy, Eu, and Tb are summarized in Table 5. The chromaticity coordinate was measured based on the corresponding photoluminescence spectrum of all the samples, and they are also represented in Fig. 19 and one of the sample YAG:DyEuTb$_{0.02}$ phosphor is represented in Fig. 6S its indicates pure white region according to NTSC.

4.11.1 Color purity analysis

Color purity of the all-synthesized sample is calculated by Eq. (16).

$$Colorpurity = \frac{\sqrt{(x - x_i)^2 + (y - y_i)^2}}{\sqrt{(x_d - x_i)^2 + (y_d - y_i)^2}} \times 100\% \quad (16)$$

Where, x and y is the CIE co-ordinate of samples, and $x_i = 0.3300$ and $y_i = 0.3300$ co-ordinate of white light. x_d and y_d Is the dominate wavelength co-ordinate samples. Calculated color purity of the samples is listed in Table 5. As we used cooping of Eu and Tb, and enhanced the concentration of Tb ions color co-ordinate are shifted toward center of white region due to enhancing intensity of blue green and red emission peak as shown in Fig. 19. The color purity of phosphor samples (YAG:DyEuTb$_{1-x}$) is calculated very less because it emits all the RGB color simultaneously. After subtraction the color purity 95.68% is calculated for YAG:DyEuTb$_{0.02}$ sample indicating the pure white color emission.

4.11.2 Correlated color temperature (CCT) analysis

McCamy formula Eq. (17) [75] is used for the calculation of CCT value of all synthesized phosphor.
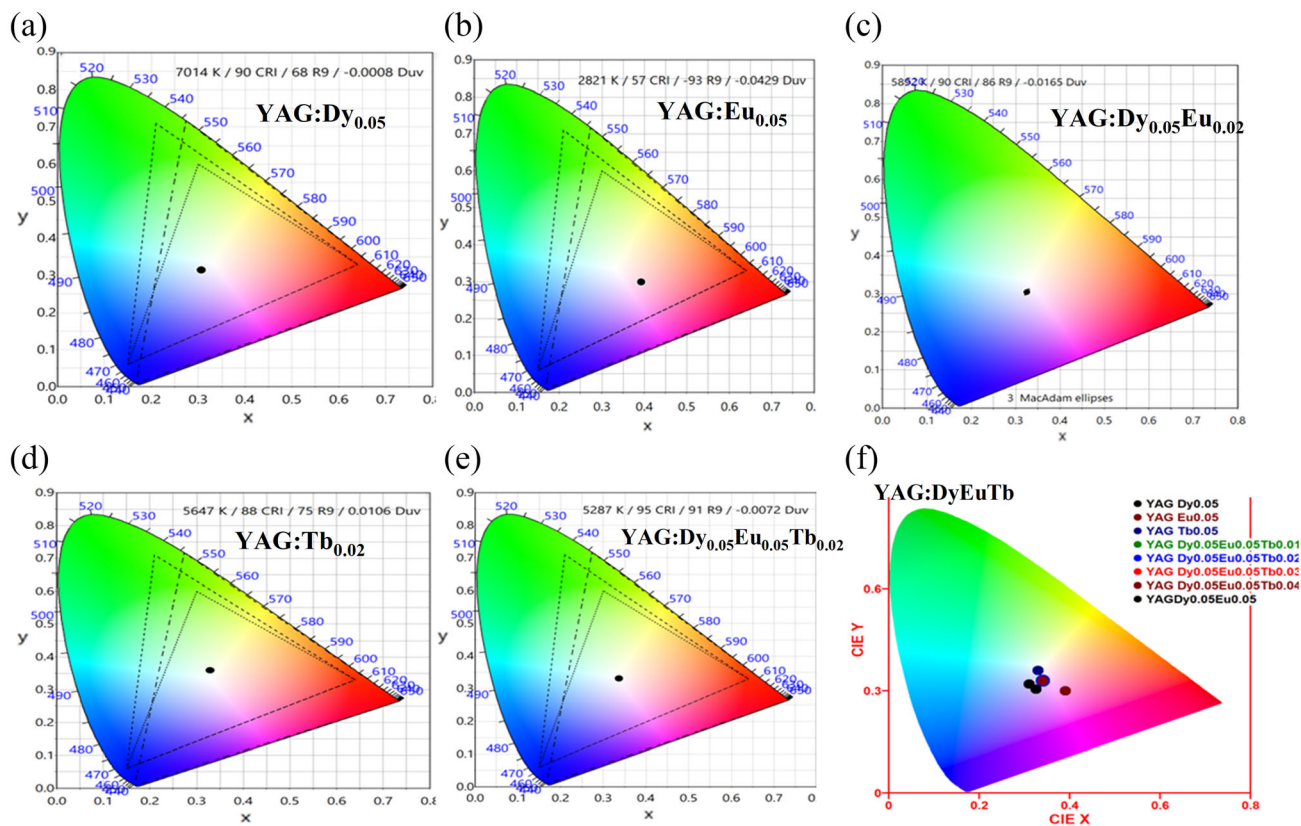

Fig. 19 The typical CIE-1931 color chromaticity image for all synthesized phosphors

$$T = -437n^3 + 3601n^2 - 6861n + 5514.31 \qquad (17)$$

$$n = \frac{x - 0.332}{y - 0.1858}$$

Where, $x_e = 0.332$, $y_e = 0.1858$ is the epicenter of convergence of the is iso-temperature lines in 1931 chromaticity diagram and x, y is CIE co-ordinate of samples. All the calculated CCT values is listed in Table 5 of the samples. Moreover, when we used cooping of Eu and Tb, and enhanced the concentration of Tb ions then CCT value is decreases with respect to concentration of sensitizer ions. The YAG:DyEuTb$_{0.02}$ of phosphor lie above the 5000 K is indicates that sample show cool appearance [58]. Therefore, the triple doped YAG sample is potential candidates (phosphor materials) for cool WLEDS.

4.11.3 Color rendering index (CRI) analysis

The quotatives measurement of the ability of a PL emission spectrum of synthesized phosphor reveals separately colors of different objects faithfully which is called CRI of the synthesized phosphor. It can compare with standard natural light source. If CRI of any light source is found range from 75 to 100 this value indicates an excellent quality of light source [76]. In this observation we were measured CRI from 90 to 95 of the synthesized phosphors. In this work, we have calculated the CRI value of all samples YAG:Dy, YAG:Eu, YAG:Tb, YAG:DyEu, YAG:DyEuTb$_{0.01}$, YAG:DyEuTb$_{0.02}$, YAG:DyEuTb$_{0.03}$, and YAG:DyEuTb$_{0.04}$. are listed in Table 5 by Ghosh Eq.(18) [77]. In this research work we have calculated 95.6 CRI value of YAG:DyEuTb$_{0.02}$ phosphor sample. This result indicates excellent value of CRI. It may be use in advance solid state lighting system, and displaying purpose.

$$CRI = \frac{1}{8}\sum_{i=1}^{8} R_i \qquad (18)$$

4.12 Quantum efficiency (Q.E.) analysis

The PL quantum efficiency (Q.E.) is a significant observation of the phosphor materials and key metric for lighting industries for the resultant of luminescent processes of LEDs, WLEDs, lamps, and displays. Ideally, this value of quantum efficiency should be 1 that indicates reduce losses of energy. The observed

Q.E. is tabulated in Table 6, and it can calculate by the Eq. (19). Where, E_{sam} = PL intensity of excitation spectra of samples, E_{ref} = PL intensity of excitation spectra of reference, $I_{sam.}$ = PL intensity of emission spectra of the samples, and. The internal (IQE) and an external quantum efficiency (EQE) were calculated by Eqs. (20) & (21) [78–80] for all synthesized samples. The IQE is always larger than the EQE shown in Table 8.

$$Q.E = \frac{I_{Sam.}}{E_{ref.} - E_{Sam.}} \qquad (19)$$

$$IQE = \frac{\gamma_{ab}}{\gamma_{ex} - \gamma_r} \qquad (20)$$

$$EQE = \frac{\gamma_{ab}}{\gamma_{ex}} \qquad (21)$$

Where, γ_{ab} is the total absorbed photons, γ_{ex} is the total emitted photons by the excitation, and γ_r is the total reflected photons and not absorbed by the sample. QE, IQE, and EQE were calculated for all samples YAG:Dy, YAG:Eu, YAG:Tb, YAG:DyEu, YAG:DyEuTb$_{0.01}$, YAG:DyEuTb$_{0.02}$, YAG:DyEuTb$_{0.03}$, and YAG:DyEuTb$_{0.04}$. In this research work, the maximum quantum is calculated for YAG:DyEuTb$_{0.02}$ (93.7%) and YAG:Dy (94.9%). Therefore, this result indicates YAG:DyEuTb$_{0.02}$ is suitable and advanced material for making WLED lighting device.

5 Conclusion

In this research work, Dy^{3+}, Eu^{3+}, Tb^{3+} singly doped, Eu^{3+}/Tb^{3+} co- doped, and Dy^{3+}/Eu^{3+}/Tb^{3+} co-doped Y$_3$Al$_5$O$_{12}$ phosphors were synthesized via combustion method. PXRD and Rietveld refinement plot of the synthesized compounds confirm that the synthesized phosphors present pure cubic structure. The average crystallite size (D_s = 15–60 nm) was observed for the YAG based samples. It is also observed that the average grain size (D_{SEM} = 50–100 nm) were about 2–3 times higher than the average crystallite size (D_{hkl}) obtained by the PXRD data of garnet-based phosphor materials. For the formation of advance white phosphor, we were used Y$_3$Al$_5$O$_{12}$ based compound activated Dy, Eu, and Tb rare earth metals. By the PL emission spectra of the Y$_3$Al$_5$O$_{12}$:Dy^{3+} Eu^{3+}Tb^{3+} exhibits blue, green, yellow, and red sharp and intense peaks due to excitation of Dy^{3+}, Eu^{3+}, and Tb^{3+} ions under the 356 nm. The

photoluminescence emission spectra, life time decay curve, energy transfer efficiency, and Reisfeld's approximation reveals the energy transfer from Dy^{3+} to Tb^{3+} and Tb^{3+} to Eu^{3+} ions. Finally, Dexter theory is concluded that the dipole-dipole interaction ($Q = 5.0784$) is responsible for this energy transfer process. The $YAG:DyEuTb_{0.02}$ has CIE co-ordinate (0.3369, 0.3312) in white region, higher luminescence color purity (95.68%), CRI (95), CCT (5287 K), and Quantum efficiency (93.7%) indicating that it has the white light emission for the WLED advanced materials for modern lighting system.

Acknowledgements

Author contributions

AK Investigation, designed the whole research, Conceptualization, synthesized all the samples, and collected experimental data, Data plotting, writing of the manuscript, review, editing and formatting, and editing of manuscript corresponding to the journals. IPS manuscript editing, thoroughly analysis and revised the articles review. DPB and NM proposed many good suggestions.

Data availability

The authors states that analyzed and relevant data of synthesized materials, which are including and described in the manuscript will be freely available to researchers and scientists who are working purpose of research and social welfare.

Declarations

Conflict of interest On behalf of all authors, the corresponding author states that there is no conflict of interest

Supplementary Information: The online version contains supplementary material available at https://doi.org/10.1007/s10854-023-10022-8.

References

1. G.B. Nair, H.C. Swart, S.J. Dhoble, A review on the advancements in phosphor converted light emitting diodes (pc-LEDs): phosphor synthesis, device fabrication and characterization. Prog. Mater. Sci. **109**, 100622 (2020). https://doi.org/10.1016/j.pmatsci.2019.100622

2. Jz. Huang, Sy. Liu, Nn. Yao, Xj. Xu, Optical properties of Eu^{3+}, Dy^{3+} co-doped ZnO nanocrystals. Optoelectron. Lett. **10**, 161–163 (2014). https://doi.org/10.1007/s11801-014-4004-z

3. H. Kang, K. Nam Lee, S. Unithrattil, H.J. Kim, J. Hye Oh, J.S. Yoo, W. Bin Im, Y. Rag do, Narrow-Band $SrMgAl_{10}O_{17}:Eu^{2+}$, Mn^{2+} green phosphors or wide-color-gamut backlight for LCD displays. ACS Omega **5**, 19516–19524 (2020). https://doi.org/10.1021/acsomega.0c01798

4. L. Wang, M. Xu, H. Zhao, D. Jia, Luminescence, energy transfer and tunable color of Ce^{3+}, Dy^{3+}/Tb^{3+} doped $BaZn_2(PO_4)_2$ phosphors. New J. Chem. **40**, 3086 (2016). https://doi.org/10.1039/c5nj03148f

5. K. Orekhova, R. Tomala, M. Zamoryanskaya, The study of composition, structure and cathodoluminescent features of $YAG:Eu^{3+}$ nanoceramics. Excitation capture efficiency of Eu^{3+} energy levels. J. Alloys Compd. **858**, 157731 (2021). https://doi.org/10.1016/j.jallcom.2020.157731

6. M. Borlaf, M. Frankowska, W.W. Kubiak, T. Graulea, Strong photoluminescence emission at low dopant amount in YAG:ce and YAG:Eu phosphors. Mater. Res. Bull. **100**, 413–419 (2018). https://doi.org/10.1016/j.materresbull.2018.01.005

7. M. Upasani, Synthesis of $Y_3Al_5O_{12}:Eu$ and $Y_3Al_5O_{12}:Eu,Si$ phosphors by combustion method: comparative investigations on the structural and spectral properties. J. Adv. Ceram. **5**(4), 344–355 (2016). https://doi.org/10.1007/s40145-016-0208-y

8. S.K. Ruan, J.G. Zhou, A.M. Zhong, J.F. Duan, X.-B. Yang, M.Z. Su, Synthesis of Y3Al5O12:Eu3+ phosphor by sol-gel method and its luminescence behavior. J. Alloys Compd. **275–277**, 72–75 (1998). https://doi.org/10.1016/S0925-8388(98)00276-X.K.M

9. S. Nissamudeen, A.H. Sankar, K.G. Bahna, Gopchandran, Studies on the influence of lithium incorporation in the photoluminescence of $Y_2O_3:Eu^{3+}$ thin films. J. Phys. Chem. Solids **70**, 821–826 (2009). https://doi.org/10.1016/j.jpcs.2009.04.002

10. S. Ray, A. Banerjee, P. Pramanik, Selective synthesis, characterization, and photoluminescence study of $YPO_4:Eu^{3+}$ nanorods and nanoparticles. Mater. Res. Bull/ **45**, 870–877 (2010). https://doi.org/10.1016/j.materresbull.2010.02.020

11. Z. Cheng, R. Xing, Z. Hou, S. Huang, J. Lin, Patterning of light-emitting $YVO_4:Eu^{3+}$ thin Films via inkjet printing.

J. Phys. Chem. C **114**, 9883–9888 (2010). https://doi.org/10.1021/jp101941y

12. K.V. Dabre, S.J. Dhoble, Synthesis and photoluminescence properties of Eu^{3+}, Sm^{3+} and Pr^{3+} doped Ca_2ZnWO_6 phosphors for phosphor converted LED. J. Lumin. **150**, 55–58 (2014). https://doi.org/10.1016/j.jlumin.2014.01.045

13. Y. Xia, Y. Huang, Q. Long, S. Liao, Y. Gao, J. Liang, J. Cai, Near-UV light excited Eu^{3+},Tb^{3+}, Bi^{3+} co-doped $LaPO_4$ phosphors: synthesis and enhancement of red emission for WLEDs. Ceram. Int. **41**, 5525–5530 (2015). https://doi.org/10.1016/j.ceramint.2014.12.128

14. V. Lojpur, S. Culubrk, M. Medic, M. Dramicanin, Luminescence thermometry with Eu^{3+} doped $GdAlO_3$. J. Lumin. **170**, 467–471 (2015). https://doi.org/10.1016/j.jlumin.2015.06.032

15. G. Annadurai, S.M.M. Kennedy, Synthesis and photoluminescence properties of Ba2CaZn2Si6O17:Eu3+ red phosphors for white LED applications. J. Lumin. **169**, 690–694 (2016). https://doi.org/10.1016/j.jlumin.2015.03.007

16. A.K. Verma, A. Verma, G.V. Bramhe, I.P. Sahu, Optical studies of the $Ba_{1-x}MgAl_{10}O_{17}:Eu_x$ phosphor synthesis by combustion route. J. Alloys Compd. **769**, 831–842 (2018). https://doi.org/10.1016/j.jallcom.2018.07.371

17. K. Kajiwara, T. Hida, K. Tanaka, Blue-emitting ZnS:Ag,Al phosphors with low defect density for high-voltage field-emission displays. J. Vac. Sci. Technol. B **21**, 515–518 (2003). https://doi.org/10.1116/1.1516183

18. V. Babin, V.V. Laguta, M. Nikl, J. Pejchal, A. Yoshikawa, S. Zazubovich, On the luminescence origin in Y_2SiO_5:ce and Lu_2SiO_5:Ce single crystals. Opt. Mater. **103**, 109832 (2020). https://doi.org/10.1016/j.optmat.2020.109832

19. X. Lan, Q. Wei, Y. Chen, W. Tang, Luminescence properties of Eu^{2+}-activated $KMg_4(PO_4)_3$ for blue-emitting phosphor. Opt. Mater. **34**, 1330–1332 (2012). https://doi.org/10.1016/j.optmat.2012.02.013

20. H.J. Song, D.K. Yim, H.S. Roh, I.S. Cho, S.J. Kim, Y.H. Jin, H.-W. Shim, D.W. Kim, K.S. Hong, RbBaPO4:Eu2+: a new alternative blue-emitting phosphor for UV-based white light-emitting diodes. J. Mater. Chem. C **1**, 500–505 (2015). https://doi.org/10.1039/c2tc00162d

21. G. Ju, Y. Hu, L. Chen, X. Wang, Z. Mu, Blue persistent luminescence in Eu^{2+} doped $Ca_3Mg_3(PO_4)_4$. Opt. Mater. **36**, 1183–1188 (2014). https://doi.org/10.1016/j.optmat.2014.02.024

22. X. Zhang, F. Mo, L. Zhou, M. Gong, Properties–structure relationship research on $LiCaPO_4$:Eu^{2+} as blue phosphor for NUV LED application. J. Alloys Compd. **575**, 314–318 (2013). https://doi.org/10.1016/j.jallcom.2013.05.188

23. J.L. Yuan, X.Y. Zeng, J.T. Zhao, Z.J. Zhang, H.H. Chen, GBin Zhang, Rietveld refinement and photoluminescent properties of a new blue-emitting material: Eu^{2+} activated

$SrZnP_2O_7$. J. Solid State Chem. **180**, 3310–3316 (2007). https://doi.org/10.1016/j.jssc.2007.09.023

24. R.L. Kohale, S.J. Dhoble, Eu^{2+} luminescence in $SrCaP_2O_7$ pyrophosphate phosphor. Luminescence **28**, 656–661 (2012). https://doi.org/10.1002/bio.2411

25. S.W. Kim, T. Hasegawa, T. Ishigaki, K. Uematsu, K. Toda, M. Sato, Efficient red emission of blue-light excitable new structure type $NaMgPO_4$:Eu^{2+} phosphor. ECS Solid State Lett. **2**, R49 (2013). https://doi.org/10.1149/2.004312ssl

26. R. Naik, S.C. Prashantha, H. Nagabhushana, H.P. Nagaswarupa, K.S. Anantharaju, S.C. Sharma, B.M. Nagabhushana, H.B. Premkumar, K.M. Girish, Mg_2SiO_4:Tb^{3+} nanophosphor: auto ignition route and near UV excited photoluminescence properties for WLEDs. J. Alloys Compd. **617**, 69–75 (2014). https://doi.org/10.1016/j.jallcom.2014.07.100

27. Z.J. Zhang, O.M. Ten Kate, A. Delsing, P. Dorenbos, J.T. Zhao, H.T. Hintzen, Photoluminescence properties of Pr^{3+}, Sm^{3+} and Tb^{3+} doped $SrAlSi_4N_7$ and energy level locations of rare-earth ions in $SrAlSi_4N_7$. J. Mater. Chem. C Mater. Opt. Electron. Devices **2**, 7952–7959 (2014). https://doi.org/10.1039/c4tc00538d

28. V. Singh, R.P.S. Chakradhar, J.L. Rao, D.-K. Kim, Mn^{2+} activated $MgSrAl_{10}O_{17}$ green emitting phosphor-A luminescence and EPR study. J. Lumin. **128**, 1474–1478 (2008). https://doi.org/10.1016/j.jlumin.2008.02.001

29. J.S. Kim, J.S. Kim, T.W. Kim, H.L. Park, Y.G. Kim, S.K. Chang et al., Energy transfer among three luminescent centers in full-color emitting $ZnGa_2O_4$:Mn^{2+}, Cr^{3+} phosphors. Solid State Commun. **131**, 493–497 (2004). https://doi.org/10.1016/j.ssc.2004.06.023

30. V.R. Panse, N.S. Kokode, K.N. Shinde, S.J. Dhoble, Luminescence in microcrystalline green emitting $Li_2Mg_{1-x}ZrO_4$:xTb^{3+}(0.1 ≤ x ≤ 2.0) phosphor. Results Phys. **8**, 99–103 (2018). https://doi.org/10.1016/j.rinp.2017.10.025

31. V. Sivakumar, A. Lakshmanan, S. Kalpana, R.S. Rani, R.S. Kumara, M.T. Jose, Low-temperature synthesis of Zn_2SiO_4:mn green photoluminescence phosphor. J. Lumin. **132**, 1917–1920 (2012). https://doi.org/10.1016/j.jlumin.2012.03.007

32. H.S. Kang, Y.C. Kang, H.D. Park, Y.G. Shul, Y_2SiO_5:tb phosphor particles prepared from colloidal and aqueous solutions by spray pyrolysis. Appl. Phys. A **80**, 347–351 (2005). https://doi.org/10.1007/s00339-003-2228-z

33. M. Upasani, Synthesis of $Y_3Al_5O_{12}$:Tb & $Y_3Al_5O_{12}$:Tb,Si phosphor by combustion synthesis: comparative investigations on the structural and spectral properties. Opt. Mater. **64**, 70–74 (2017). https://doi.org/10.1016/j.optmat.2016.11.039

34. J.J. Joos, J. Botterman, P.F. Smet, Evaluating the use of blue phosphors in white LEDs: the case of

$Sr_{0.25}Ba_{0.75}Si_2O_2N_2:Eu^{2+}$. J. Solid State Light **1**, 6 (2014). https://doi.org/10.1186/2196-1107-1-6

35. L. Chen, C.-C. Lin, C.-W. Yeh, R.S. Liu, Light converting inorganic phosphors for white light-emitting diodes. Materials **3**(3), 2172–2195 (2010). https://doi.org/10.3390/ma3032172

36. C.N. George, A.K. Denault, R. Seshadri, Phosphors for solid-state white lighting. Annu. Rev. Mater. Res. **43**, 481–501 (2013). https://doi.org/10.1146/annurev-matsci-073012-125702

37. K.S. Dhoble, J.A. Wani, S.J. Dhoble, NUV excited $K_2SrP_2O_7:RE^{3+}$ (RE = sm, tb, Eu, Dy) phosphors for white light generation. Adv. Mater. Lett. **7**(9), 765–769 (2016). https://doi.org/10.5185/amlett.2016.6182

38. M. Shang, D. Geng, Y. Zhang, G. Li, D. Yang, X. Kang, J. Lin, Luminescence and energy transfer properties of Ca8Gd2(PO4)6O2:(Ce3+/Eu2+/Tb3+/Dy3+/Mn2+) phosphors. J. Mater. Chem. **22**, 19094 (2012). https://doi.org/10.1039/c2jm34092e

39. J.A. Dorman, J.H. Choi, G. Kuzmanich, J.P. Chang, High-quality white light using core-shell $RE^{3+}:LaPO_4$ (RE = Eu, Tb, Dy, Ce) phosphors. J. Phys. Chem. C **116**, 12854–12860 (2012). https://doi.org/10.1021/jp300858z

40. T.S. Dhapodkar, A.R. Kadam, N. Brahme, S.J. Dhoble, Efficient white light-emitting $Mg_{21}Ca_4Na_4(PO_4)_{18}$: Dy^{3+}, Tb^{3+}, Eu^{3+} triple-doped glasses: a multipurpose glass for WLEDs, solar cell efficiency enhancement, and smart windows applications. Mater. Today Chem. **24**, 100938 (2022). https://doi.org/10.1016/j.mtchem.2022.100938

41. P.S. Mbule, B.M. Mothudi, M.S. Dhlamini, $Mn^{2+}-Eu^{3+}-Dy^{3+}$ doped and co-doped Zn_2SiO_4 nanophosphors: study of the structure, photoluminescence and surface properties. J. Lumin. **192**, 853–859 (2017). https://doi.org/10.1016/j.jlumin.2017.08.020

42. B. Fan, W. Zhao, L. Han, Eu^{3+} co–doped $Sr_3Gd(PO_4)_3:Dy^{3+}$ phosphors: luminescence properties and color–tunable white–light emission for NUV–WLEDs. Appl. Phys. A **126**, 260 (2020). https://doi.org/10.1007/s00339-020-3444-5

43. L. Zhang, Z. Lu, P. Han, L. Wang, Q. Zhang, Effective red compensation of Sr2SiO4: Dy3+ phosphor by codoping Mn2+ ions and its energy transfer. J. Nanomater. (2012). https://doi.org/10.1155/2012/848274

44. D. Valiev, T. Han, V. Vaganov, S. Stepanov, The effect of Ce3+ concentration and heat treatment on the luminescence efficiency of YAG phosphor. J. Phys. Chem. Solids **116**, 1–6 (2018). https://doi.org/10.1016/j.jpcs.2018.01.007

45. L. Wang, L. Zhuang, H. Xin, Y. Huang, D. Wang, Semi-quantitative estimation of Ce^{3+}/Ce^{4+} ratio in $YAG:Ce^{3+}$ phosphor under different sintering atmosphere. Open J. Inorg. Chem. **05**, 12–18 (2015). https://doi.org/10.4236/ojic.2015.51003

46. Y. Liu, J. Zou, M. Shi, B. Yang, Y. Han, W. Li, Z.M. Wang, H.Y. Zhou, M.T. Li, N. Jiang, Effect of gallium ion content on thermal stability and reliability of YAG: ce phosphor films for white LEDs. Ceram. Int. **44**, 1091–1098 (2018). https://doi.org/10.1016/j.ceramint.2017.10.056

47. Y. Zhao, H. Xu, X. Zhang, G. Zhu, D. Yan, A. Yu, Facile synthesis of $YAG:Ce^{3+}$ thick films for phosphor converted white light emitting diodes. J. Eur. Ceram. Soc. **35**, 3761–3764 (2015). https://doi.org/10.1016/j.jeurceramsoc.2015.05.017

48. Y. Pan, M. Wu, Q. Su, Tailored photoluminescence of YAG:ce phosphor through various methods. J. Phys. Chem. Solids **65**, 845–850 (2004). https://doi.org/10.1016/j.jpcs.2003.08.018

49. B. Wang, H. Qi, H. Han, Z. Song, J. Chen, J. Shao, Structural, luminescent properties and chemical state analysis of YAG:ce nanoparticle-based films. Opt. Mater. Exp. **6**, 155–165 (2016). https://doi.org/10.1364/OME.6.000155

50. A.H. Wako, F.B. Dejene, H.C. Swart, Effect of Ga^{3+} and Gd^{3+} ions substitution on the structural and optical properties of Ce^{3+}-doped yttrium aluminium garnet phosphor nanopowders. Luminescence **31**, 1313–1320 (2016). https://doi.org/10.1002/bio.3108

51. G.B. Nair, S.J. Dhoble, Assessment of electron-vibrational interaction (EVI) parameters of $YAG:Ce^{3+}$, $TAG:Ce^{3+}$ and $LuAG:Ce^{3+}$ garnet phosphors by spectrum fitting method. Spectrochim. Acta A Mol. Biomol. Spectroscopy **173**, 822–826 (2017). https://doi.org/10.1016/j.saa.2016.10.049

52. K. Zhang, W. Hu, Y. Wu, H. Liu, Photoluminescence investigations of $(Y_{1-x}Ln_x)_3Al_5O_{12}$:ce $(Ln^{3+},Gd^{3+},La^{3+})$ nanophosphors. Phys. B Condens. Matter **403**, 1678–1681 (2008). https://doi.org/10.1016/j.physb.2007.09.084

53. J.F.C. Carreira, N. Ben Sedrine, T. Monteiro, L. Rino, YAG:Dy-Based single white light emitting phosphor produced by solution combustion synthesis. J. Lumin. **183**, 251–258 (2017). https://doi.org/10.1016/j.jlumin.2016.11.017

54. S. Agarwal, M.S. Haseman, A. Khamehchi, P. Saadatkia, D.J. Winarski, F.A. Selim, Physical and optical properties of ce:YAG nanophosphors and transparent ceramics and observation of novel luminescence phenomenon. Opt. Mater. Exp. **7**(3), 1055–1065 (2017). https://doi.org/10.1364/OME.7.001055

55. V. Lisitsyn, L. Lisitsyna, A. Tulegenova, Y. Ju, E. Polisadova, E. Lipatov, V. Vaganov, Nano defects in YAG:Ce-based phosphor microcrystals. Crystals **9**(9), 476 (2019). https://doi.org/10.3390/cryst9090476

56. H. Shi, C. Zhu, J. Huang, J. Chen, D. Chen, W. Wang, F. Wang, Y. Cao, X. Yuan, Luminescence properties of YAG:ce, Gd phosphors synthesized under vacuum condition and their

white LED performances. Opt. Mater. Exp. **4**(4), 649–655 (2014). https://doi.org/10.1364/OME.4.000649

57. A.K. Verma, D.P. Bisen, S. Nema, I.P. Sahu, T. Ray, N. Brahme, A. Verma, A.K. Singh, Investigation of structural, luminescence, and antibacterial properties of novel Zn_{1-x}-$Eu_xAl_{2-y}O_4Sr_y$ phosphor. J. Mater. Sci: Mater. Electron. **33**, 15858–15878 (2022). https://doi.org/10.1007/s10854-022-08486-1

58. A.K. Verma, S.K. Pathak, A. Verma, G.V. Bramhe, I.P. Sahu, Tuning of luminescent properties of $Zn_{1-x}MgAl_{10}O_{17}:Eu_x$ nano phosphor. J. Alloys Compd. **764**, 1021–1032 (2018). https://doi.org/10.1016/j.jallcom.2018.06.023

59. A.K. Verma, A. Verma, G.V. Bramhe, Shifting and enhanced photoluminescence performance of the $Sr_{1-x}Eu_xMgAl_{10}O_{17}$ phosphor. J. Alloys Compd. **769**, 1168–1180 (2019). https://doi.org/10.1016/j.jallcom.2018.09.166

60. V. Singh, R.P.S. Chakradhar, J.L. Rao, H.-Y. Kwak, Photoluminescence and EPR studies of $BaMgAl_{10}O_{17}:Eu^{2+}$ phosphor with blue-emission synthesized by the solution combustion method. J. Lumin. **131**(8), 1714–1718 (2011). https://doi.org/10.1016/j.jlumin.2011.03.030

61. A.K. Verma, A. Verma, Synthesis, characterization, mechanoluminescence, thermoluminescence, and antibacterial properties of $SrMgAl_{10}O_{17}:Eu$ phosphor. J. Alloys Compd. **802**, 394–408 (2019). https://doi.org/10.1016/j.jallcom.2019.06.209

62. G.K. Williamson, W.H. Hall, X-ray line broadening from filed aluminium and wolfram. Acta Metall. **1**(1), 22–31 (1953). https://doi.org/10.1016/0001-6160(53)90006-6

63. K.D. Liss, A. Bartels, A. Schreyer, H. Clemens, X. High-Energy, Rays: a tool for advanced bulk investigations in materials science and physics. Texture Microstruct. **35**(3–4), 219–252 (2003). https://doi.org/10.1080/07303300310001634952

64. J.C. Wurst, J.A. Nelson, Lineal intercept technique for measuring grain size in two-phase polycrystalline ceramics. J. Am. Ceram. Soc. **55**(2), 109 (1972). https://doi.org/10.1111/j.1151-2916.1972.tb11224.x

65. T. Delgado, J. Afshania, H. Hagemann, Spectroscopic study of a single crystal of $SrAl_2O_4:Eu^{2+}:Dy^{3+}$. J. Phys. Chem. C **123**(14), 8607–8613 (2019). https://doi.org/10.1021/acs.jpcc.8b12568

66. B. Devakumar, P. Halappa, C. Shivakumara, Dy^{3+}/Eu^{3+} co-doped $CsGd(MoO_4)_2$ phosphor with tunable photoluminescence properties for near-UV WLEDs applications. Dyes Pigment **137**, 244–255 (2017). https://doi.org/10.1016/j.dyepig.2016.10.016

67. C. Zhu, J. Wang, M. Zhang, X. Ren, J. Shen, Y. Yue, Eu, Tb-, and Dy-doped oxyfluoride silicate glasses for LED applications. J. Am. Ceram. Soc. **97**(3), 854–861 (2014). https://doi.org/10.1111/jace.12714

68. U.H. Kaynara, S.C. Kaynarb, Y. Alajlanic, M. Ayvaciklid, E. Karalie, Y. Karabulutd, S. Akcaf, T. Karalie, N. Canb, Eu^{3+} and Dy^{3+} doped La_2MoO_6 and $La_2Mo_2O_9$ phosphors: synthesis and luminescence properties. Mater. Res. Bull. **123**, 110723 (2020). https://doi.org/10.1016/j.materresbull.2019.110723

69. M. Inokuti, F. Hirayama, Influence of energy transfer by the exchange mechanism on donor luminescence. J. Chem. Phys. **43**, 1978 (1965). https://doi.org/10.1063/1.1697063

70. P. Dharmaiah, C.S. Dwaraka Viswanath, Ch. Basavapoornima, K. Venkata Krishnaiaha, C.K. Jayasankara, S.J. Hong, Luminescence and energy transfer in Dy^{3+}/Tb^{3+} co-doped transparent oxyfluorosilicate glass-ceramics for green emitting applications. Mater. Res. Bull. **83**, 507–514 (2016). https://doi.org/10.1016/j.materresbull.2016.06.044

71. H. Li, Y. Liang, S. Liu, W. Zhang, Y. Bi, Y. Gong, Y. Chen, W. Lei, Highly efficient green-emitting phosphor $Sr_4Al_{14}O_{25}:Ce,Tb$ with low thermal quenching and wide color gamut upon UV-light excitation for backlighting display applications. J. Mater. Chem. C **9**, 2569–2581 (2021). https://doi.org/10.1039/d0tc04618c

72. N. Guo, Y. Huang, H. You, M. Yang, Y. Song, K. Liu, Y. Zheng, $Ca_9Lu(PO_4)_7:Eu^{2+},Mn^{2+}$:a potential single-phased white-light-emitting phosphor suitable for white-light-emitting diodes. Inorg. Chem. **49**, 10907–10913 (2010). https://doi.org/10.1021/ic101749g

73. T. Do, N.M. Tien, L. Son, Van Tuat, L.N. Liem, Energy transfer between Ce^{3+}- Dy^{3+} In $Ca_2Al_2SiO_7$: Ce^{3+}, Dy^{3+} Phosphor, IOP Conference Series: Materials Science and Engineering 540 (1) (2019) 012001. https://doi.org/10.1088/1757-899X/540/1/012001

74. T. Richhariya, N. Brahme, D.P. Bisen, T. Badapanda, A. Choubey, Y. Patle, E. Chandrawanshi, Synthesis and optical characterization of Dy^{3+} doped barium alumino silicate phosphor. Mater. Sci. Eng.: B **273**, 115445 (2021). https://doi.org/10.1016/j.mseb.2021.115445

75. C.S. McCamy, Correlated color temperature as an explicit function of chromaticity coordinates. Color Res. Appl. **17**, 142–144 (1992). https://doi.org/10.1002/col.5080170211

76. Y.N. Ahn, K.D. Kim, G. Anoop, G.S. Kim, J.S. Yoo, Design of highly efficient phosphor converted white light-emitting diodes with color rendering indices (R1 – R15) ≥ 95 for artificial lighting. Sci. Rep. **9**, 16848 (2019). https://doi.org/10.1038/s41598-019-53269-0

77. A. Ghosh, P. Selvaraj, S. Sundaram, T.K. Mallick, The colour rendering index and correlated colour temperature of dye-sensitized solar cell for adaptive glazing application. Sol.

Energy **163**, 537–544 (2018). https://doi.org/10.1016/j.solener.2018.02.021

78. J.C. De Mello, H.F. Wittmann, R.H. Friend, An improved experimental determination of external photoluminescence quantum efficiency. Adv. Mater. **9**(3), 230–232 (1997). https://doi.org/10.1002/adma.19970090308

79. A. Armin, M. Velusamy, P. Wolfer, Y. Zhang, P.L. Burn, P. Meredith, A. Pivrikas, Quantum efficiency of organic solar cells: electro-optical cavity considerations. ACS Photonics **1**, 173–181 (2014). https://doi.org/10.1021/ph400044k

80. A.L.N. Stevels, A.D. Schrama-de Pauw, Eu^{2+} luminescence in hexagonal aluminates containing large divalent or trivalent cations. J. Electrochem. Soc. **123**(5), 691–697 (1976). https://doi.org/10.1149/1.2132911